nature biotechnology

Article

https://doi.org/10.1038/s41587-024-02282-4

In vivo AAV–SB-CRISPR screens of tumor-infiltrating primary NK cells identify genetic checkpoints of CAR-NK therapy

Received: 18 October 2023

Accepted: 10 May 2024

Published online: 25 June 2024

Check for updates

Lei Peng[1,2,3,16], Paul A. Renauer[1,2,3,4,5,16], Giacomo Sferruzza[1,2,3], Luojia Yang[1,2,3,4,5], Yongji Zou[1,2,3], Zhenghao Fang[1,2,3], Jonathan J. Park[1,2,3,4,5,6], Ryan D. Chow[1,2,3,4,5,6], Yueqi Zhang[1,2,3], Qianqian Lin[1,2,3], Meizhu Bai[1,2,3], Angelica Sanchez[1,2,3,7], Yongzhan Zhang[1,2,3], Stanley Z. Lam[1,2,3], Lupeng Ye[1,2,3,15,17] & Sidi Chen[1,2,3,4,5,6,8,9,10,11,12,13,14,17]

Natural killer (NK) cells have clinical potential against cancer; however, multiple limitations hinder the success of NK cell therapy. Here, we performed unbiased functional mapping of tumor-infiltrating NK (TINK) cells using in vivo adeno-associated virus (AAV)–SB (Sleeping Beauty)-CRISPR (clustered regularly interspaced short palindromic repeats) screens in four solid tumor mouse models. In parallel, we characterized single-cell transcriptomic landscapes of TINK cells, which identified previously unexplored subpopulations of NK cells and differentially expressed TINK genes. As a convergent hit, *CALHM2*-knockout (KO) NK cells showed enhanced cytotoxicity and tumor infiltration in mouse primary NK cells and human chimeric antigen receptor (CAR)-NK cells. *CALHM2* mRNA reversed the *CALHM2*-KO phenotype. *CALHM2* KO in human primary NK cells enhanced their cytotoxicity, degranulation and cytokine production. Transcriptomics profiling revealed *CALHM2*-KO-altered genes and pathways in both baseline and stimulated conditions. In a solid tumor model resistant to unmodified CAR-NK cells, *CALHM2*-KO CAR-NK cells showed potent in vivo antitumor efficacy. These data identify endogenous genetic checkpoints that naturally limit NK cell function and demonstrate the use of *CALHM2* KO for engineering enhanced NK cell-based immunotherapies.

Natural killer (NK) cells are critical components of innate immunity[1,2]. The rapid and efficient cytolysis and cytokine production of NK cells make them an attractive therapeutic cell type[3]. Chimeric antigen receptor (CAR)-NK therapy[4,5], compared to conventional CAR-T cell therapies, can use allogeneic NK sources without concern of graft-versus-host disease (GVHD) and can also use CAR-independent mechanisms of cancer elimination in tumors with antigen loss[4,6]. CAR-NK therapy has shown clinical trial success against blood cancers[5,7,8] and early potential against solid tumors[9,10]. A recent trial of CD19–interleukin 15 (IL-15) CAR-NK showed a robust overall response (OR) with no notable toxicities such as cytokine release syndrome, neurotoxicity or GVHD[11], highlighting the effectiveness and exceptional safety of allogeneic CAR-NK therapy[9,10].

However, current NK cell-based immunotherapy candidates face a number of obstacles, for example, paucity[12], lower proliferative capacity and, in particular, decreased effectiveness, persistence or tumor infiltration[13–16]. Various methods have been used to improve the antitumor efficacy of NK cells, including ex vivo activation, expansion

A full list of affiliations appears at the end of the paper. e-mail: lupeng.ye@gmail.com; sidi.chen@yale.edu

and genetic modifications[17]. Only a small number of genes have been shown to date where the knockout (KO) or perturbation has had a strong effect on the antitumor efficacy of NK cells, such as *CISH*[18]. Such endogenous inhibitors (or cellular checkpoints) naturally limit the antitumor function of NK cells (such as activation, proliferation, repression of inhibitory signals, exhaustion, persistence or tumor infiltration) and, therefore, have fundamental implications for NK cell-based cancer immunotherapy.

To date, there is no reported unbiased screen in primary NK cells. CRISPR (clustered regularly interspaced short palindromic repeats) screens have been performed in cancer cells cocultured with unmodified NK cells[19–21], which identified important regulators of the cancer cell response to NK cell killing but not NK cell-intrinsic cellular checkpoints. The lack of primary NK cell screens may be because of a number of technological challenges, particularly the balance of gene-editing efficiency in primary NK cells and the scalability of the editing platform for high-throughput screens.

Here, we harnessed our efficient and scalable chimeric adeno-associated virus (AAV)–SB (Sleeping Beauty)-CRISPR system[22], which enables bona fide efficient gene editing in primary NK cells and is rapidly scalable to high-throughput screens. We performed in vivo AAV–SB-CRISPR screens directly in primary NK cells for tumor infiltration, in four different syngeneic tumor models in fully immunocompetent mice. Furthermore, we characterized the transcriptomic landscapes of tumor-infiltrating NK (TINK) cells through single-cell RNA sequencing (scRNA-seq). The in vivo screens and scRNA-seq jointly identified *CALHM2*/*Calhm2* as a convergent hit. We found that in vitro KO of *CALHM2*/*Calhm2* in mouse primary NK cells, human primary NK cells and CAR-NK cells augmented NK cell functions. Overexpressed *CALHM2* in the *CALHM2*-KO human NK cell line rescued *CALHM2*-KO phenotypes in vitro. Our results further suggested that *CALHM2*/*Calhm2*-KO NK cells exhibited superior antitumor efficacy in vivo. Our findings indicated that *CALHM2* is a promising target for enhancing NK cell-based cellular immunotherapy against cancer.

Results

In vivo AAV–SB-CRISPR mouse primary NK tumor infiltration screen

We performed in vivo CRISPR KO screens directly in mouse primary NK cells using a custom, high-density single-guide RNA (sgRNA) library (Surf-v2) in four different tumor mouse models: B16F10 melanoma, E0771 triple-negative breast cancer, GL261 glioblastoma and Pan02 pancreatic cancer (Fig. 1a and Methods). We selected these tumor models with available syngeneic lines for a spectrum of clinically relevant cancer types. For the screen readout, we extracted genomic DNA (gDNA) from NK cells before injection and at 7 days after adoptive transfer from the tumors and spleens of tumor-bearing animals (Fig. 1a). We then analyzed infiltration screen perturbation maps using MAGeCK-RRA (Methods)[23], which identified specific sets of enriched sgRNAs over nontargeting controls (NTCs) and mutant genes in the TINK cells in each of the four tumor models (Fig. 1b and Supplementary Dataset 1). Notable hits included *Plxna1*, *Sort1*, *Itga2*, *Tlr4*, *Adra2c*, *Lrrn4*, *Klrk1*, *Tnfrsf18 (Gitr)*, *Tnfrsf22*, *Ccr10*, *Slc4a5*, *Pcdhb1*, *Cd40lg*, *Enpp1*, *Lrp1*, *Spn*, *Mrc1*, *Slc34a2* and *Calhm2* (Fig. 1b). By comparing the screen hits with gene expression data from the ImmGen project (Methods)[24], we showed that the majority of these genes are naturally expressed in peripheral primary NK cells (147 of 156, 94%) (Supplementary Fig. 1).

Single-cell transcriptomics of TINK cells

To gain independent global functional maps of NK cells in the tumor microenvironment (TME), we performed scRNA-seq of TINK cells. From the orthotopic syngeneic tumor models engrafted by B16F10 or E0771 cells in B6 mice, we isolated tumor and spleen NK cells at 7 and 15 days after injection by fluorescence-assisted cell sorting (FACS) and subjected them to single-cell transcriptomics profiling using the 10x Genomics platform (Fig. 1c and Supplementary Datasets 2–4). Pretransfer donor NK cells were also sequenced in parallel to serve as a control or baseline while exploring the effects of time, tumor type and tissue localization on NK cell phenotype (Supplementary Fig. 2a). We generated a total of eight different scRNA-seq datasets, represented by the various factors of time, tumor type and tissue localization (Supplementary Fig. 2a). Data were integrated[25], analyzed (Methods) and visualized in a reduced dimensional space using uniform manifold approximation and projection (UMAP) (Supplementary Fig. 2a)[26] and cell populations were clustered by the transcription patterns of highly variable genes (Supplementary Fig. 2b,c). NK and innate lymphoid cell (ILC) populations were filtered by Ncr1$^+$ expression and then classified by the expression of known cell-type-specific markers (Supplementary Figs. 2c and 3a,b). We detected one group of NK T cells (*Ncr1*$^+$*Cd3e*$^+$), one group of ILC1 cells (*Ncr1*$^+$*Rora*$^+$*Gpr183*$^+$*Cxcr6*$^+$) and nine groups of NK cells, which we further characterized on the basis of signature gene expression markers (Fig. 1d,e, Supplementary Figs. 3c and 4a,b and Supplementary Dataset 2). Notably, these NK cell subsets included mature NK (mNK), tissue-resident NK (trNK) and proliferative NK (NK5) cells (Fig. 1e and Supplementary Fig. 4a,b). We also identified signatures of effector responses in mNK cells, regulatory responses in NK1, trNK, ILC1 and NK T cells and both responses in the NK3, NK4 and NK6 cell subsets (Supplementary Fig. 4b). The characteristic expression patterns of the NK cell subsets were relatively stable across conditions; however, some transcription factors had time-specific signatures, such as *Rora, Zeb2* and *Tcf7* expression at early time points. There was also tissue-specific expression of key genes, including spleen-predominant expression of mNK cell markers (Supplementary Fig. 4b).

We further compared the NK cell subtypes using differential expression (DE) and pathway analyses, which showed decreased effector and killing responses in NK1 and trNK cells, increased differentiation

Fig. 1 | In vivo AAV–SB-CRIPSR NK cell screen and scRNA-seq of TINK cells jointly identified *Calhm2* as a convergent gene for NK cell engineering. **a**, Schematic of the in vivo AAV–SB-Surf-v2 CRISPR KO screens for NK cell tumor infiltration, performed in four independent syngeneic tumor models. **b**, Dot plot of the screen analysis results, presented by rank and significance ($-\log_{10}$ (*P* value)). Data were analyzed using the MAGeCK algorithm and top hits (colored points) are labeled. **c**, Schematic for the single-cell transcriptomic exploration of NK cells within the tumor and spleen of two different in vivo cancer models across multiple time points. **d**, UMAP plot of NK subset populations across eight integrated single-cell transcriptomic datasets. Cells are color-labeled according to their original dataset, including pretransfer donor NK cells (controls) and NK cells from different time points, tumor models and tissues. **e**, Violin plots of the expression of select NK phenotype gene signatures, compared across different NK subset populations. The gene signatures represent the scaled sum of normalized expression across multiple key genes for each NK subset. **f**, Volcano plots of DE analyses for B16F10 and E0771 tumor infiltration of NK single-cell data. DE analyses were performed using single-cell expression data fitted to generalized linear models (shown at bottom) and quasi-likelihood *F* tests that assessed tumor infiltration as a coefficient. Upregulated and downregulated genes are shown by red and blue dots, respectively ($q < 0.01$, absolute $\log_2$(FC) > 1) and the top gene names are presented for each. **g**, Network plots of meta-pathway analysis results for DE genes from the B16F10 and E0771 tumor infiltration analyses of NK single-cell expression data. Pathways were analyzed with the g:Profiler2 R package using either upregulated or downregulated genes (indicated on plots) in the indicated DE analysis. Significantly enriched pathways (points) were plotted by similarity, clustered and labeled by a representative pathway (meta-pathway) (Methods). The top six meta-pathways are shown for each plot. **h**, Venn diagram showing the identification of *Calhm2* as a convergent target from in vivo screens, peripheral NK gene expression and loss of gene expression in TINK cells (scRNA-seq). Statistical details can be found in the Supplementary Information.

https://doi.org/10.1038/s41587-024-02282-4

a NK cell tumor infiltration in vivo CRISPR screen

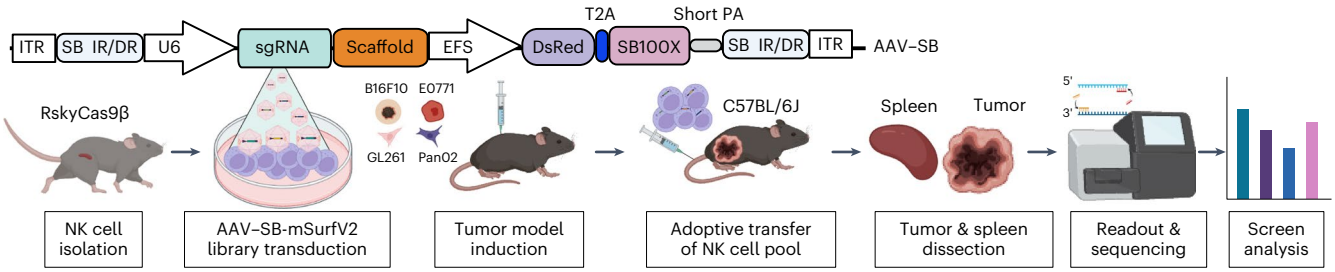

b MAGeCK screen analysis

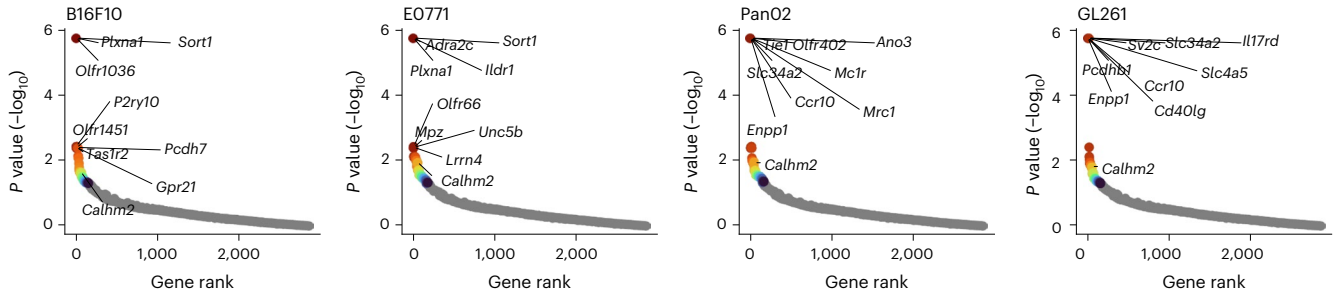

c Tumor-infiltrating NK cell scRNA-seq

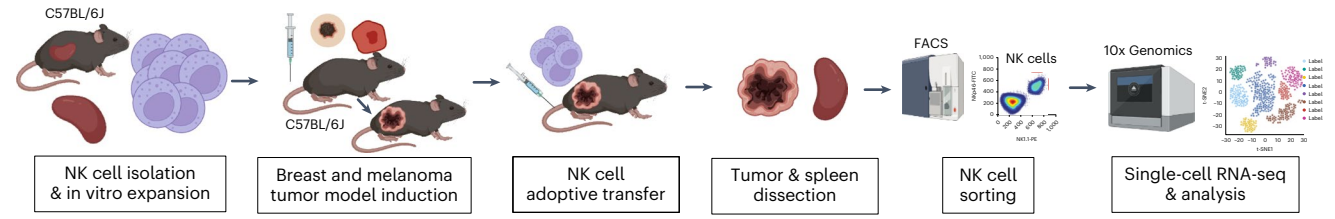

d Single-cell analysis of Ncr1+ cells

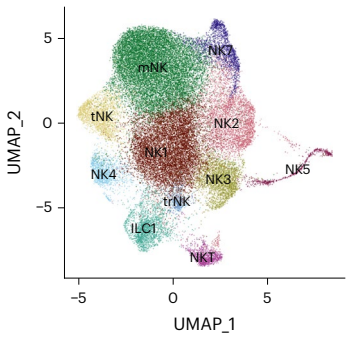

e Gene expression signatures

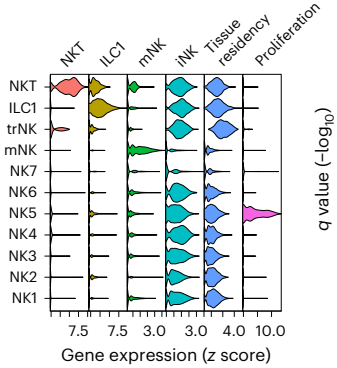

f

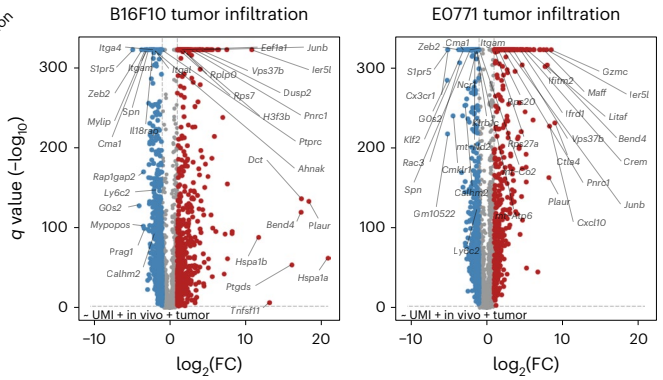

g

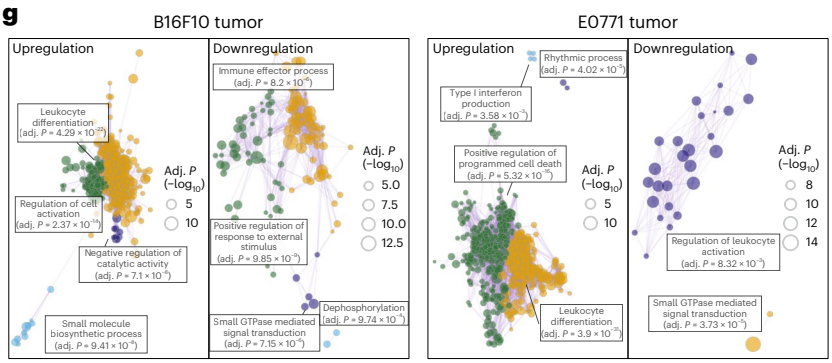

h

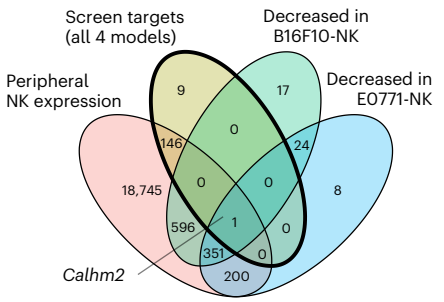

in NK2 cells, decreased cytokine-related pathways in NK3 and NK7 cells, increased effector immune response pathways in NK4 and NK5 cells, increased mitosis in NK5 cells and increased chemotaxis in NK6 cells (Supplementary Fig. 5a,b). To identify the regulators of these NK subtype signatures, we looked at the top DE transcriptional regulators (GO:0140110) of each NK subset and demonstrated relatively specific expression of several factors, including *Rora* in ILC1 cells, *Klf2* and *Zeb2* in mNK cells, *Batf3* in trNK cells, high *Nr4a1* and *Rel* in NK6 cells, *Hmgb2* and *Ezh2* in NK5 cells and *Ifi204, Stat1* and *Irf7* in NK4 cells (Supplementary Fig. 5c).

NK subpopulation changes in progressing tumors

We analyzed NK cell subpopulations in B16F10 and E0771 models (Methods) and found that the vast majority of NK cell subsets were highly stable across all conditions (Supplementary Fig. 6a). NK4 cells were the only NK subset specifically localized within the tumor (Supplementary Fig. 6a). The NK2 cell population also exhibited tumor-specific trends and its presence was significantly associated with the preinjection in vitro cell culture conditions, given the decreased presence in each tumor model, over time and in the spleen and tumor extracts (Supplementary Fig. 6a). We also observed an increasing abundance of mNK cells in spleen and tumor extracts as compared to preinjection cells (Supplementary Fig. 6a).

Gene expression in TINK subpopulations

The transcriptional programs of tumor infiltration were explored across all NK cell populations by DE analysis. The top upregulated genes in B16F10 and E0771 included the activation gene *Junb* and senescence-related *Litaf* gene[27] (Fig. 1f and Supplementary Dataset 3), while the top downregulated genes included mNK cell markers and genes involved in terminal NK differentiation, such as *Zeb2*, *Spn*, *Ly6c2* and *S1pr5* (ref. 28) (Fig. 1f and Supplementary Fig. 6b). Although there were significantly more mNK cells in the spleen than in the tumor, this finding was still unexpected, given that the TINK population comprised ~20% mNK cells (Supplementary Fig. 6a). Across tumor NK subtypes, there was significant correlation of the gene expression in either tumor model (Supplementary Fig. 6c). Separate DE analyses of tumor infiltration by each NK subset also showed similar patterns across each tumor model (Supplementary Fig. 7a), although there were tumor-specific differences, including increased *S100a8/9* expression in all E0771-infiltrating NK subsets and increased *Ly6a* expression in all but the NK5 E0771 NK subsets (Supplementary Fig. 7b). Meta-pathway analyses revealed significantly enriched meta-pathways such as those involved in differentiation, leukocyte activation, apoptosis and immune responses (Fig. 1g and Supplementary Dataset 4).

C*alhm2* KO enhanced mouse primary NK function

We analyzed the intersection of CRISPR screen hits, DE genes from single-cell profiling and genes that are naturally expressed in peripheral blood primary NK cells. *CALHM2*/*Calhm2* was the only gene that emerged as the common hit (scored in the screen, expressed in non-tumor primary NK cells and downregulated in TINK cells from both cancer models) (Fig. 1h). Notably, our single-cell data demonstrated decreased *Calhm2* average expression and gene detection rates in tumor samples for most of the NK subpopulations (Supplementary Fig. 8a–c). Overall, *Calhm2* expression was predominantly found in the spleen NK subsets and was largely lost in the TINK subsets (Supplementary Fig. 8a–c). While the role of *Calhm2*/*CALHM2* in NK cells is unclear, it was found to regulate the proinflammatory activity of microglial cells and is a potential therapeutic target for diseases related to microglia-mediated neuroinflammation[29,30].

We first investigated how CALHM2 protein expression levels were affected by activation in mouse primary NK cells. Western blot analyses revealed that CALHM2 protein expression was relatively low in freshly isolated mouse primary NK cells and significantly upregulated in expanded NK cells (Supplementary Fig. 9a). Following stimulation with cancer cells (YAC-1-PL (YAC-1 expressing the puromycin–luciferase transgene), 1:1 ratio, 48 h), the CALHM2 protein level was significantly decreased in primary NK cells (Supplementary Fig. 9a), consistent with our results from scRNA-seq analysis. These data suggest that CALHM2 protein levels were modulated in NK cells, in both in vitro and in vivo settings.

We then examined the effect of *Calhm2* KO in mouse NK cells, again using our AAV–SB-CRISPR system with NK cells isolated from Cas9$^+$ mice. *Calhm2*-KO NK cells showed reduced CALHM2 protein levels, which was verified by western blot (Supplementary Fig. 9b). We quantified NK cell proliferation using cell-trace dye assays and found that *Calhm2* KO did not influence mouse primary NK cell proliferation at multiple time points, ranging from 24 to 168 h (Supplementary Fig. 9c). We then investigated whether *Calhm2* influences tumor infiltration by tracking the number of *Calhm2*-KO CD45.2 donor NK cells in CD45.1 host mice with orthotopic E0771 tumors. At 48 h after transfer, we showed that *Calhm2* KO significantly increased donor CD45.2$^+$ NK cell numbers in the tumor, while having no effect on NK cell numbers in the spleen (Supplementary Fig. 9d,e, top and bottom panels). We also assessed the in vitro cytotoxicity of *Calhm2*-KO NK cells using coculture assays with different cancer cell lines, including an NK-sensitive YAC-1-PL line and the four cell lines used in our screens (E0771-PL, B16F10-PL, Pan02-PL and GL261-PL). Our results showed that *Calhm2*-KO NK cells had significantly enhanced cytolysis against all cell lines tested (at an effector-to-target cell (E:T) ratio of 1:1), relative to vector control NK cells (Supplementary Fig. 9f).

CALHM2 KO enhanced CAR-NK92 antitumor function

We then characterized the effect of *CALHM2* deficiency in a clinically applicable human NK cell line, NK92 (ref. 31), which has been widely used for CAR-NK studies and has entered clinical trials[32,33]. We generated

Fig. 2 | *CALHM2* KO in CAR-NK92 enhanced tumor infiltration and antitumor efficacy in vitro and in vivo. a, Schematic of the generation of anti-HER2-CAR-hIL-2-NK92 cells with *CALHM2* and *AAVS1* editing and efficacy testing with in vitro coculture and in vivo tumor. **b**, *CALHM2* gene editing in NK92, evaluated using the T7E1 assay ($n = 1$). **c**, Protein-level knockdown of CALHM2 in CAR-NK92 cells, measured by western blot ($n = 3$). **d**, Proliferation in *CALHM2*-KO anti-HER2-CAR-hIL-2-NK92 cells. Left, histogram plot. Right, relative mean fluorescence intensity (MFI) quantification ($n = 4$). **e**, Schematic of in vivo tumor infiltration assay of *CALHM2*-KO anti-HER2-CAR-hIL-2-NK92 cells. **f**, Flow cytometry quantification of TINK cells in mice treated with *CALHM2*-KO versus *AAVS1*-KO anti-HER2-CAR-hIL-2-NK92 cells at 2 and 9 days after treatment (days 21 and 28, respectively). **g**, Cytotoxicity evaluation of *CALHM2*-KO anti-HER2-CAR-hIL-2-NK92 cells toward MCF-7-PL-HER2-OE, MCF-7-PL and HT29-GL cells ($n = 3$–4). **h**, Enhanced cytotoxicity of *CALHM2*-KO anti-HER2-CAR-hIL-2-NK92 cells toward HT29-GL cells ($n = 3$). **i**, Degranulation (CD107a) quantification of *CALHM2*-KO versus *AAVS1*-KO anti-HER2-CAR-hIL-2-NK92 cells ($n = 3$) upon stimulation with cancer cells. **j**, Schematic for in vivo tumor cytotoxicity analysis. **k**, Tumor growth curve of HT29-GL tumor-bearing mice treated with PBS ($n = 4$ mice), *CALHM2*-KO ($n = 5$ mice) or *AAVS1*-KO ($n = 5$ mice) anti-HER2-CAR-hIL-2-NK92 cells. **l**, Timeline of *CALHM2* rescue experiments. **m**, CALHM2 protein expression in *CALHM2*-KO anti-HER2-CAR-hIL-2-NK92 cells, measured by western blot ($n = 3$). **n**, Cytotoxicity measurements of CALHM2-OE in *CALHM2*-KO anti-HER2-CAR-hIL-2-NK92 cells toward HT29-GL ($n = 6$) and MDA-MB231-PL cells ($n = 6$). **o**, Degranulation (CD107a) quantification of CALHM2-OE in *CALHM2*-KO anti-HER2-CAR-hIL-2-NK92 cells responding to HT29-GL ($n = 3$–4) and MDA-MB231-PL ($n = 4$) cell stimulation. Data are shown as the mean ± s.e.m. plus individual data points in dot plots. Statistical significance was evaluated using unpaired two-sided *t*-tests for the majority of panels. In **d**,**h**,**k**, a two-way analysis of variance was used to assess statistical significance with multiple testing comparisons. The statistical significance levels are indicated in the plots (****$P < 0.0001$, ***$P < 0.001$, **$P < 0.01$ and *$P < 0.05$).

https://doi.org/10.1038/s41587-024-02282-4

CALHM2-mutant NK92 cells by Cas9 guide RNA (gRNA) ribonucleoprotein (RNP) electroporation (Fig. 2a). We verified gene editing in the *CALHM2* locus using the T7EI assay (Fig. 2b) and protein-level knockdown of CALHM2 by western blot (Fig. 2c).

We then tested other anticancer features of *CALHM2* KO in several different versions of NK92 or CAR-NK92 cells. We tested the effect of *CALHM2* loss in parental NK92 cells. The *CALHM2*-KO group showed significantly increased cytotoxicity toward multiple cell lines in coculture

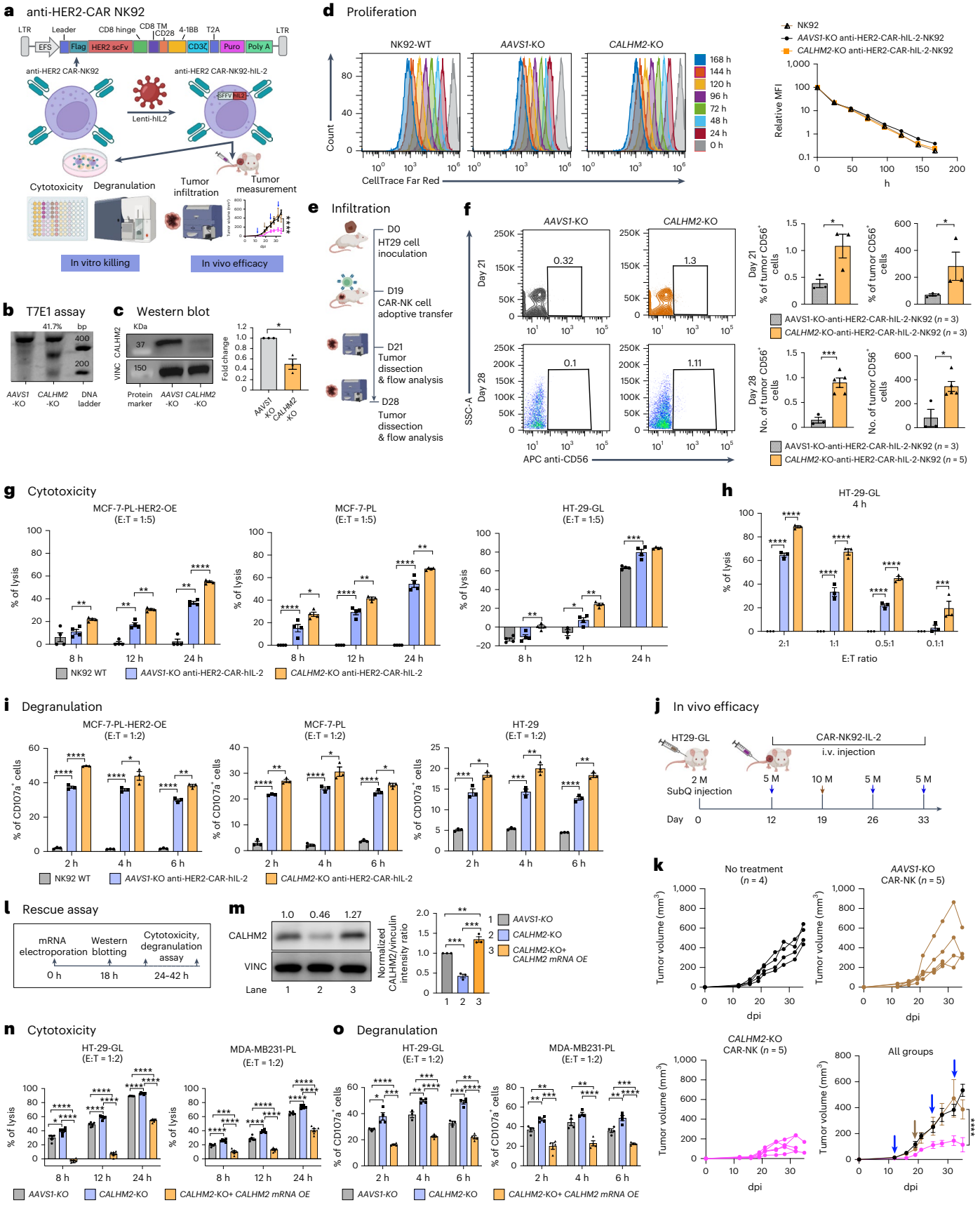

assays, including an NK cell-sensitive leukemia cancer cell line K562, as well as solid tumor cell lines HT29 and MDA-MB231 (Supplementary Fig. 10a). To further investigate whether *CALHM2* can serve as an endogenous gene target to enhance CAR-NK function, we established both anti-BCMA (B cell maturation antigen) CAR-NK92 and anti-HER2 (human epidermal growth factor receptor 2) CAR-NK92 cells to study the effect of *CALHM2* KO (Methods). We tested the surface protein-level expression of the cognate CAR antigen BCMA in a panel of cell lines, confirming their antigen specificity in relevant multiple myeloma (MM) lines (Supplementary Fig. 10b,c). Lentiviral CAR transduction and puromycin selection allowed us to generate high-purity (97.6–99.1%) anti-BCMA-CAR-NK92 cells (Supplementary Fig. 10d). Coculture assays showed that *CALHM2*-KO anti-BCMA-CAR-NK92 cells had higher cytotoxicity than the *AAVS1*-KO control toward MM.1R-PL-BCMA-OE (*BCMA*-overexpressing MM.1R, a B lymphoblast cell line from a person with MM, with the PL reporter genes) cells at different E:T ratios (Supplementary Fig. 10e). Similarly, we tested the surface protein-level expression of the HER2 antigen in a panel of cell lines, confirming their antigen specificity in relevant solid tumor lines (Supplementary Fig. 10f,g). We generated high-purity (94–95.6%) anti-HER2-CAR-NK92 cells (Supplementary Fig. 10h). Coculture assays showed that *CALHM2*-KO anti-HER2-CAR-NK92 cells had enhanced cytotoxicity toward multiple lines of HER2$^+$ cells at two different E:T ratios across different time points (Supplementary Fig. 10i). Degranulation assays showed that *CALHM2*-KO anti-HER2-CAR-NK92 cells had higher levels of CD107a after stimulation by cognate HER2$^+$ MCF-7-HER2-OE cancer cells (Supplementary Fig. 11a).

As NK92 cells are human (h)IL-2 dependent[34], we established anti-HER2-CAR-NK92-hIL-2 cells by lentiviral delivery to assess the antitumor function and the effect of *CALHM2* KO, both in vitro and in vivo (Fig. 2a). We quantified the proliferation using cell-trace dye assays. Results showed that *CALHM2* KO did not influence anti-HER2-CAR-hIL-2-NK92 cell proliferation at multiple time points, ranging from 24 to 168 h (Fig. 2d). We evaluated tumor infiltration and persistence in vivo using a solid tumor model, induced by subcutaneous injection of a human colon cancer cell line HT29-GL (HT29 expressing the green fluorescent protein–luciferase transgene) (Fig. 2e). Results showed that *CALHM2* KO increased CAR-NK infiltration at 21 days post tumor implantation (dpi), corroborated with data from a longer time point (28 dpi) (Fig. 2f). Coculture assays showed that *CALHM2* KO significantly enhanced the cytotoxicity of anti-HER2-CAR-NK92-hIL-2 cells toward HER2$^+$ MCF-7-PL-HER2-OE, MCF-7-PL and HT29-GL cancer cells (Fig. 2g). Furthermore, *CALHM2* KO significantly enhanced the cytotoxicity of anti-HER2-CAR-NK92-hIL-2 cells toward HT29-GL cells at four different E:T ratios (Fig. 2h). Degranulation assays showed that *CALHM2*-KO anti-HER2-CAR-hIL-2-NK92 cells had higher levels of CD107a after stimulation by cognate HER2$^+$ MCF-7-PL-HER2-OE, MCF-7-PL and HT29-GL cancer cells (Fig. 2i and Supplementary Fig. 11b, c). We then tested the efficacy of *CALHM2*-KO anti-HER2-CAR-NK92-hIL-2 cells in vivo using a solid tumor model (HT29-GL xenograft in NSG mice) (Fig. 2j). The tumor growth curve data that control (*AAVS1*-targeted) anti-HER2-CAR-hIL-2-NK92 cells had no notable in vivo efficacy against HT29 tumors (Fig. 2k), reminiscent of the resistance of solid tumors to current CAR-NK therapy without further genetic modifications. In sharp contrast, tumor growth kinetics showed that *CALHM2*-KO anti-HER2-CAR-hIL-2-NK92 cells had potent in vivo antitumor efficacy (Fig. 2k). Together, these in vitro and in vivo data demonstrated that *CALHM2* perturbation significantly enhanced the antitumor activities of human CAR-NK92 cells, including cytotoxicity, degranulation, infiltration and overall antitumor efficacy.

CALHM2 transgene rescued *CALHM2*-KO phenotypes

To further validate the causality of the *CALHM2*-KO effect in NK cells, we conducted a rescue experiment by reintroducing the *CALHM2* gene product into *CALHM2*-KO anti-HER2-CAR-hIL-2-NK92 cells. We generated a *CALHM2*-OE transgene, produced *CALHM2* mRNA by in vitro transcription and electroporated the *CALHM2* mRNA into *CALHM2*-KO anti-HER2-CAR-hIL-2-NK92 cells, resulting in successful overexpression of the CALHM2 protein as confirmed by western blot (Fig. 2l,m). Subsequent in vitro cytotoxicity assays revealed that *CALHM2* overexpression significantly attenuated the heightened cancer-killing capability observed in *CALHM2*-KO anti-HER2-CAR-hIL-2-NK92 cells in two cancer lines (HT29 and MDA-MB-231) across three time points (Fig. 2n). Of note, the overexpression effect was found to be stronger than the wild type (WT; *AAVS1* control group), potentially because of the higher level of CALHM2 protein in the overexpression NK92 cells as compared to WT cells with an endogenous level of CALHM2. Degranulation assays also demonstrated that CALHM2 overexpression reduced the production of CD107a in *CALHM2*-KO anti-HER2-CAR-hIL-2-NK92 cells upon encountering HT29 or MDA-MB-231 cancer cells at three different time points (Fig. 2o). These results further affirmed that the phenotypic effects of *CALHM2* were caused by *CALHM2* KO and could be reversed by transgene rescue.

CALHM2 KO enhanced human primary NK cell functions

To further expand the utility of CALHM2 targeting in the engineering of more clinically relevant NK cell therapy, we extended the characterization of *CALHM2* KO in human primary NK cells. We isolated and expanded human primary NK cells from the peripheral blood of three distinct healthy human donors with K562-mIL-21-4-1BBL-mIL-15 feeder cells (Fig. 3a) (Methods). We further purified the NK cell population (CD56$^+$CD3$^-$) by bead selection (>90% purity) (Fig. 3b). Using CRISPR RNP electroporation, we functionally knocked out *CALHM2* in human primary NK cells from all three donors, as confirmed by western blot, although the levels of CALHM2 protein knockdown varied among donors (Fig. 3c,e,g). In vitro coculture assays showed that *CALHM2* KO significantly augmented NK cell cytotoxic killing against different cancer cell lines (including the K562-GL leukemia line and solid tumor lines HT29-GL and MCF-7-PL) with different E:T ratios across all three independent donors (Fig. 3d,f,h and Supplementary Fig. 12a–c).

To robustly confirm the effects of *CALHM2* KO, we assessed two different CRISPR RNAs (crRNAs) that target distinct sites within the *CALHM2* gene (crRNA1 and crRNA2), both of which decreased CALHM2 protein levels (Fig. 3g). We performed coculture assays with

Fig. 3 | *CALHM2* KO in human primary NK cells enhanced antitumor function. **a**, Schematic representation of the expansion and gene editing of human PBMC-derived primary NK (PB-NK) cells. **b**, Assessment of purity in PB-NK cells after 7 days of expansion with feeder cells and purification with bead selection. **c**, Protein-level knockdown of CALHM2 in PB-NK cells (donor 1; $n = 3$ replicates), measured by western blot. **d**, Cytotoxicity of *CALHM2*-KO and *AAVS1*-KO control PB-NK cells (donor 1) toward K562-GL ($n = 5$ each) or HT29-GL ($n = 5$ each) cancer cells at 8 h with varying E:T ratios. **e**, Protein-level knockdown of CALHM2 in PB-NK cells (donor 2; $n = 3$ replicates), measured by western blot. **f**, Cytotoxicity of *CALHM2*-KO and *AAVS1*-KO control PB-NK cells (donor 2) toward K562-GL ($n = 3$ each) or HT29-GL ($n = 4$ each) cancer cells at 8 h with varying E:T ratios. **g**, Protein-level knockdown of CALHM2 in PB-NK cells (donor 3; $n = 3$ replicates) using two different crRNAs (crRNA1 and crRNA2), measured by western blot. **h**, Cytotoxicity of *CALHM2*-KO (crRNA1 or crRNA2) and *AAVS1*-KO control PB-NK cells (donor 3) toward K562-GL ($n = 3$ each) or HT29-GL ($n = 3$ each) cancer cells at 8 h. **i**, Degranulation of *CALHM2*-KO and *AAVS1*-KO control *CALHM2*-KO PB-NK cells (donor 1) upon stimulation with K562 ($n = 3$ each) or HT29 ($n = 3$ each) cancer cells. **j**, IFNγ and TNFα production of *CALHM2*-KO and *AAVS1*-KO control PB-NK cells (donor 1) after 12 h of stimulation with K562-GL ($n = 3$–4 replicates) or HT29-GL ($n = 3$–4 replicates) cancer cells. Data are shown as the mean ± s.e.m. plus individual data points in dot plots. Statistical significance was evaluated using unpaired two-sided *t*-tests for the majority of panels. The statistical significance levels are indicated in the plots (****$P < 0.0001$, ***$P < 0.001$, **$P < 0.01$ and *$P < 0.05$).

https://doi.org/10.1038/s41587-024-02282-4

the *CALHM2*-KO primary human NK cells (isolated from donor 3) generated by these two crRNAs and observed consistently enhanced in vitro cytolysis of cancer cells for *CALHM2*-KO NK cells generated by either crRNA (Fig. 3h).

Furthermore, we assessed degranulation and found that *CALHM2*-KO primary human NK cells exhibited increased production of CD107a upon stimulation with K562 or HT29 cancer cells at 2 and 4 h (Fig. 3i). Enhanced effector cytokine (interferon-γ (IFNγ) and tumor necrosis factor-α

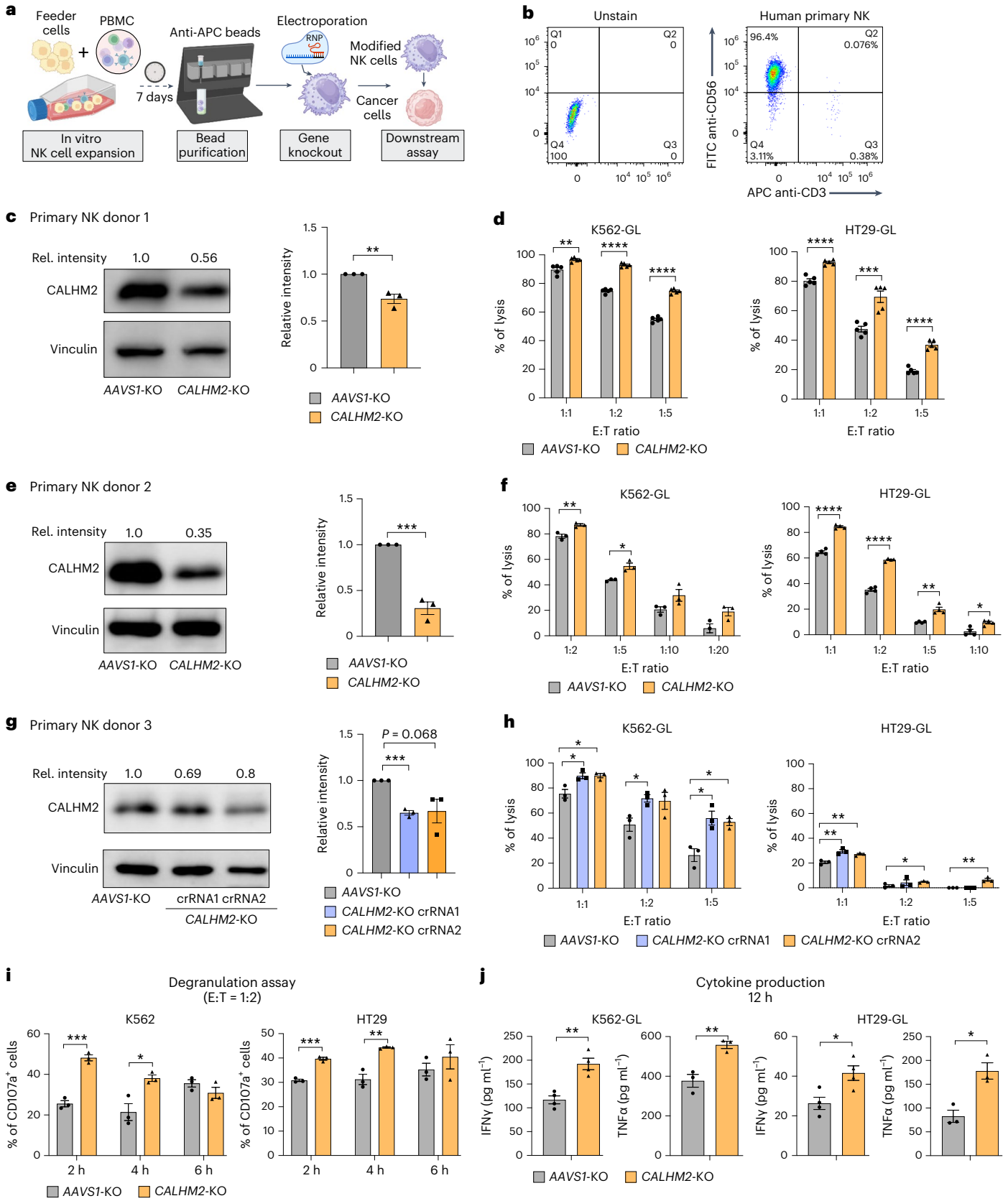

https://doi.org/10.1038/s41587-024-02282-4

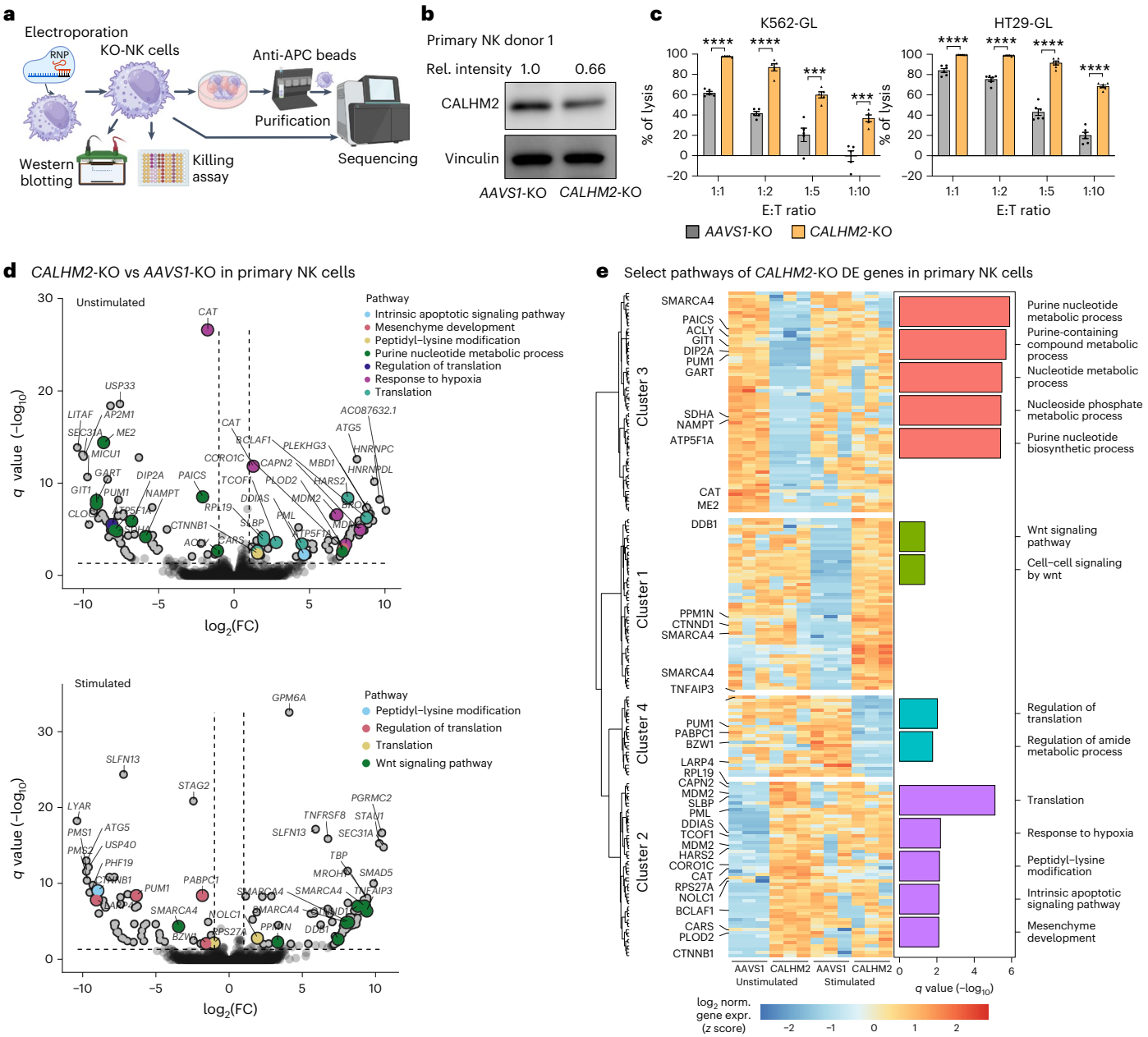

Fig. 4 | *CALHM2* KO altered multiple pathways in human primary NK cells. **a**, Schematic representation of gene editing and RNA-seq analysis of human PBMC-derived NK cells. **b**, Protein-level knockdown of CALHM2 in primary NK cells, measured by western blot. This experiment was conducted once. **c**, Cytotoxicity of *CALHM2*-KO and *AAVS1*-KO control human primary NK cells against K562-GL ($n = 5–6$) and HT29-GL ($n = 6$) cancer cells at 8 h with different E:T ratios. **d**, Volcano plots from the DE analysis of *CALMH2*-KO versus *AAVS1*-KO control NK cells at baseline and after 6 h of activation ($n = 3$ replicates per group). DE transcripts are shown by dots, color-coded by the top pathways shown in **e**, and the top significant DE transcripts are labeled with their gene symbols. The vertical dashed lines represent the thresholds of $\log_2$(FC) at −1 and 1, while the horizontal dashed line represents the *q* value threshold of 0.05. **e**, Heat map of DE genes (absolute $\log_2$(FC) > 1 and $q < 0.05$) from the analysis of *CALMH2*-KO versus *AAVS1*-KO control NK cells at baseline and after 6 h of activation. DE genes were clustered hierarchically ($k = 4$) by *z* scores and pathway analyses were performed on DE genes from each cluster, as shown by the bar plot. Only ≤5 significantly enriched pathways are presented from each cluster. Statistical significance was evaluated using unpaired two-sided *t*-tests for the majority of panels. The statistical significance levels are indicated in the plots (****$P < 0.0001$, ***$P < 0.001$, **$P < 0.01$ and *$P < 0.05$).

(TNFα)) production was also observed in *CALHM2*-KO primary human NK cells after 12-h stimulation with different cancer cell lines including K562, HT29 and MCF-7 (Fig. 3j and Supplementary Fig. 12d). These data collectively demonstrated that *CALHM2* KO consistently enhanced the cytotoxicity, effector cytokine production and degranulation of human primary NK cells against several cell lines of multiple cancer cell types, further supporting *CALHM2* targeting as a means for engineering more effective, clinically relevant, primary human NK cells against cancer.

CALHM2 KO alters multiple pathways in human primary NK cells

As the gene regulation underlying *CALHM2* in NK cells is largely unknown, to reveal in an unbiased manner how *CALHM2* perturbation changes downstream genes, we performed bulk mRNA-seq in *CALHM2*-KO (*CALHM2* gRNA) and control (*AAVS1* gRNA) human peripheral-blood-derived NK cells at rest (baseline, unstimulated condition) and after 6 h of stimulation with HT29-GL cells (stimulated

condition) (Fig. 4a and Supplementary Dataset 5). We confirmed CALHM2 protein downregulation and increased cancer lysis from the bulk mRNA-seq results of *CALHM2*-KO human primary NK cells (Fig. 4b,c). mRNA libraries were prepared using the same set of NK cell samples.

Using the edgeR DE pipeline[35] (Methods), the *CALHM2*-KO effect in primary NK cells revealed 98 upregulated and 96 downregulated gene transcripts in resting NK cells and 114 upregulated and 60 downregulated gene transcripts in activated NK cells (absolute $\log_2$(fold change (FC)) > 1 and false discovery rate (FDR)-adjusted $P < 0.05$) (Fig. 4d,e). To explore which downstream pathways are altered in *CALHM2* KO, we clustered DE genes from our analyses of resting and activated NK cells and performed pathway analyses on the gene clusters (Fig. 4e). We identified four clusters of DE genes: stimulated-CALHM2-up (cluster 1), stimulated-CALHM2-down (cluster 4), baseline-CALHM2-up (cluster 2) and baseline-CALHM2-down (cluster 3). The results revealed multiple new enriched pathways of genes downstream of *CALHM2* KO in baseline and stimulated conditions.

We predominantly observed enriched pathways related to stress response and cell death in *CALHM2*-KO NK cells. The upregulated genes in resting *CALHM2*-KO NK cells were associated with translation changes, as well as pathways of hypoxia response and intrinsic apoptotic signaling (Fig. 4d,e). At baseline (unstimulated), *CALHM2*-KO NK cells had stronger stress response gene expression (hypoxia response) and upregulated antiapoptotic genes, such as *MDM2*, *DDIAS*, *CTNNB1* and *PML*, along with other relevant genes, such as *NKG2D*, *LITAF* and *ATG5*. Under stimulated conditions, *CAHLM2*-KO NK cells had higher Wnt signaling pathway gene expression (Fig. 4d,e), such as *CTNND1, PPM1N, DDB1, SMARCA4* and *TNFAIP3*. TNFAIP3 (TNFα-induced protein 3) negatively regulates nuclear factor (NF)-κB signaling in NK cells. The downregulated genes in stimulated *CALHM2*-KO NK cells were associated with the regulation of translation, including *LARP4* and *PABPC1*. These data together suggested that *CALHM2* KO led to notable changes in several sets of important downstream genes and pathways in human primary NK cells.

Discussion

NK cells have strong potential as cancer immunotherapies[36,37]. Therapeutic NK cells can be manufactured as allogeneic or off-the-shelf products and recent clinical trials showed that CAR-NK cells have similar efficacy with substantially lower toxicity compared to CAR-T cell therapies[11]. However, NK cell-based immunotherapies have their own challenges, in which the NK cell functions are naturally limited by endogenous genetic suppressors. This requires modification of endogenous genes to enhance NK cell potency against cancer. Several existing approaches, including overexpression of cytokines ('armored' fourth-generation CAR-NK cells) such as IL-15 (ref. 11) and KO of negative regulators such as *CISH*[18,38], have shown notable functional enhancements of cord-blood-derived CAR-NK cells. However, the number of currently known or identified NK cell checkpoints is scarce. To systematically identify genes that suppress NK function and, therefore, CAR-NK therapy, we performed in vivo pooled AAV–SB-CRISPR KO screens directly in mouse primary NK cells that were introduced to fully immunocompetent syngeneic tumor models. We also used an orthogonal unbiased approach, scRNA-seq, to identify subpopulations and gene signatures of TINK cells in the TME. We identified *CALHM2*/*Calhm2* as a convergent hit from both datasets. *CALHM2* KO significantly increased the cytotoxicity, degranulation, cytokine production and tumor infiltration of primary NK cells and CAR-NK cells. Targeting *CALHM2* rendered human anti-HER2-CAR-NK92 cells more capable of overcoming solid tumor resistance and robustly improved in vivo efficacy. It should be noted that, unlike simple cytokine overexpression, the approach of knocking out endogenous checkpoints such as *CALHM2* requires gene editing, which may involve a more complex manufacturing process for CAR-NK therapy. In the future, gain-of-function screens based on CRISPR activation or open reading frames may be used to identify functional boosters in CAR-NK cells, which are easier to engineer as therapeutic cell products. In summary, this study's in vivo AAV–SB-CRISPR screen and TINK scRNA-seq identified endogenous genes that likely serve as genetic checkpoints to naturally inhibit NK function. Targeting these suppressor genes, such as *CALHM2*, offers a promising means to engineer new enhanced NK cell therapies against cancer.

Online content

Any methods, additional references, Nature Portfolio reporting summaries, source data, extended data, supplementary information, acknowledgements, peer review information; details of author contributions and competing interests; and statements of data and code availability are available at https://doi.org/10.1038/s41587-024-02282-4.

References

1. Vivier, E., Tomasello, E., Baratin, M., Walzer, T. & Ugolini, S. Functions of natural killer cells. *Nat. Immunol.* **9**, 503–510 (2008).
2. Ben-Shmuel, A., Biber, G. & Barda-Saad, M. Unleashing natural killer cells in the tumor microenvironment-the next generation of immunotherapy? *Front. Immunol.* **11**, 275 (2020).
3. Hu, W., Wang, G., Huang, D., Sui, M. & Xu, Y. Cancer immunotherapy based on natural killer cells: current progress and new opportunities. *Front. Immunol.* **10**, 1205 (2019).
4. Elahi, R., Heidary, A. H., Hadiloo, K. & Esmaeilzadeh, A. Chimeric antigen receptor-engineered natural killer (CAR NK) cells in cancer treatment; recent advances and future prospects. *Stem Cell Rev. Rep.* **17**, 2081–2106 (2021).
5. Marofi, F. et al. CAR-NK cell: a new paradigm in tumor immunotherapy. *Front. Oncol.* **11**, 673276 (2021).
6. Marofi, F. et al. Renaissance of armored immune effector cells, CAR-NK cells, brings the higher hope for successful cancer therapy. *Stem Cell Res. Ther.* **12**, 200 (2021).
7. Albinger, N., Hartmann, J. & Ullrich, E. Current status and perspective of CAR-T and CAR-NK cell therapy trials in Germany. *Gene Ther.* **28**, 513–527 (2021).
8. Rezvani, K. CD19 CAR NK-cell therapy in leukemia & lymphoma. *Oncol. Times* **42**, 35 (2020).
9. Wrona, E., Borowiec, M. & Potemski, P. CAR-NK cells in the treatment of solid tumors. *Int. J. Mol. Sci.* **22**, 5899 (2021).
10. Portillo, A. L. et al. Expanded human NK cells armed with CAR uncouple potent anti-tumor activity from off-tumor toxicity against solid tumors. *iScience* **24**, 102619 (2021).
11. Marin, D. et al. Safety, efficacy and determinants of response of allogeneic CD19-specific CAR-NK cells in $CD19^+$ B cell tumors: a phase 1/2 trial. *Nat. Med.* **30**, 772–784 (2024).
12. Abel, A. M., Yang, C., Thakar, M. S. & Malarkannan, S. Natural killer cells: development, maturation, and clinical utilization. *Front. Immunol.* **9**, 1869 (2018).
13. Myers, J. A. & Miller, J. S. Exploring the NK cell platform for cancer immunotherapy. *Nat. Rev. Clin. Oncol.* **18**, 85–100 (2021).
14. Shimasaki, N., Jain, A. & Campana, D. NK cells for cancer immunotherapy. *Nat. Rev. Drug Discov.* **19**, 200–218 (2020).
15. Cózar, B. et al. Tumor-infiltrating natural killer cells. *Cancer Discov.* **11**, 34–44 (2021).
16. Ge, Z., Wu, S., Zhang, Z. & Ding, S. Mechanism of tumor cells escaping from immune surveillance of NK cells. *Immunopharmacol. Immunotoxicol.* **42**, 187–198 (2020).
17. Chu, J. et al. Natural killer cells: a promising immunotherapy for cancer. *J. Transl. Med.* **20**, 240 (2022).
18. Bernard, P. L. et al. Targeting CISH enhances natural cytotoxicity receptor signaling and reduces NK cell exhaustion to improve solid tumor immunity. *J. Immunother. Cancer* **10**, e004244 (2022).

19. Pan, R., Ryan, J., Pan, D., Wucherpfennig, K. W. & Letai, A. Augmenting NK cell-based immunotherapy by targeting mitochondrial apoptosis. *Cell* **185**, 1521–1538 (2022).
20. Sheffer, M. et al. Genome-scale screens identify factors regulating tumor cell responses to natural killer cells. *Nat. Genet.* **53**, 1196–1206 (2021).
21. Chiba, M. et al. Genome-wide CRISPR screens identify CD48 defining susceptibility to NK cytotoxicity in peripheral T-cell lymphomas. *Blood* **140**, 1951–1963 (2022).
22. Ye, L. et al. In vivo CRISPR screening in CD8 T cells with AAV–Sleeping Beauty hybrid vectors identifies membrane targets for improving immunotherapy for glioblastoma. *Nat. Biotechnol.* **37**, 1302–1313 (2019).
23. Li, W. et al. MAGeCK enables robust identification of essential genes from genome-scale CRISPR/Cas9 knockout screens. *Genome Biol.* **15**, 554 (2014).
24. ImmGen, C. Open-source ImmGen: mononuclear phagocytes. *Nat. Immunol.* **17**, 741 (2016).
25. Stuart, T. et al. Comprehensive integration of single-cell data. *Cell* **177**, 1888–1902 (2019).
26. Becht, E. et al. Dimensionality reduction for visualizing single-cell data using UMAP. *Nat. Biotechnol.* **37**, 38–44 (2019).
27. Pfefferle, A. et al. Intra-lineage plasticity and functional reprogramming maintain natural killer cell repertoire diversity. *Cell Rep.* **29**, 2284–2294 (2019).
28. van Helden, M. J. et al. Terminal NK cell maturation is controlled by concerted actions of T-bet and Zeb2 and is essential for melanoma rejection. *J. Exp. Med.* **212**, 2015–2025 (2015).
29. Cheng, J. et al. Microglial Calhm2 regulates neuroinflammation and contributes to Alzheimer's disease pathology. *Sci. Adv.* **7**, eabe3600 (2021).
30. Choi, W., Clemente, N., Sun, W. N., Du, J. & Lu, W. The structures and gating mechanism of human calcium homeostasis modulator 2. *Nature* **576**, 163–167 (2019).
31. Nowakowska, P. et al. Clinical grade manufacturing of genetically modified, CAR-expressing NK-92 cells for the treatment of ErbB2-positive malignancies. *Cancer Immunol. Immunother.* **67**, 25–38 (2018).
32. Boyiadzis, M. et al. Phase 1 clinical trial of adoptive immunotherapy using "off-the-shelf" activated natural killer cells in patients with refractory and relapsed acute myeloid leukemia. *Cytotherapy* **19**, 1225–1232 (2017).
33. Williams, B. A. et al. A phase I trial of NK-92 cells for refractory hematological malignancies relapsing after autologous hematopoietic cell transplantation shows safety and evidence of efficacy. *Oncotarget* **8**, 89256–89268 (2017).
34. Tam, Y. K. et al. Characterization of genetically altered, interleukin 2-independent natural killer cell lines suitable for adoptive cellular immunotherapy. *Hum. Gene Ther.* **10**, 1359–1373 (1999).
35. Lun, A. T., Chen, Y. & Smyth, G. K. It's DE-licious: a recipe for differential expression analyses of RNA-seq experiments using quasi-likelihood methods in edgeR. *Methods Mol. Biol.* **1418**, 391–416 (2016).
36. Vivier, E. et al. Natural killer cell therapies. *Nature* **626**, 727–736 (2024).
37. Dagher, O. K. & Posey, A. D. Jr. Forks in the road for CAR T and CAR NK cell cancer therapies. *Nat. Immunol.* **24**, 1994–2007 (2023).
38. Daher, M. et al. Targeting a cytokine checkpoint enhances the fitness of armored cord blood CAR-NK cells. *Blood* **137**, 624–636 (2021).

[1]Department of Genetics, Yale University School of Medicine, New Haven, CT, USA. [2]System Biology Institute, Yale University, West Haven, CT, USA. [3]Center for Cancer Systems Biology, Yale University, West Haven, CT, USA. [4]Combined Program in the Biological and Biomedical Sciences, Yale University, New Haven, CT, USA. [5]Molecular Cell Biology, Genetics, and Development Program, Yale University, New Haven, CT, USA. [6]M.D.-Ph.D. Program, Yale University, West Haven, CT, USA. [7]Yale College, Yale University, New Haven, CT, USA. [8]Immunobiology Program, Yale University, New Haven, CT, USA. [9]Yale Comprehensive Cancer Center, Yale University School of Medicine, New Haven, CT, USA. [10]Department of Neurosurgery, Yale University School of Medicine, New Haven, CT, USA. [11]Yale Stem Cell Center, Yale University School of Medicine, New Haven, CT, USA. [12]Yale Liver Center, Yale University School of Medicine, New Haven, CT, USA. [13]Yale Center for Biomedical Data Science, Yale University School of Medicine, New Haven, CT, USA. [14]Yale Center for RNA Science and Medicine, Yale University School of Medicine, New Haven, CT, USA. [15]Present address: Nanjing University, Nanjing, China. [16]These authors contributed equally: Lei Peng, Paul A. Renauer. [17]These authors jointly supervised this work: Lupeng Ye, Sidi Chen. ✉e-mail: lupeng.ye@gmail.com; sidi.chen@yale.edu

Methods

Institutional approval

This study received institutional regulatory approval. All recombinant DNA and biosafety work was performed under the guidelines of the Yale Environment, Health and Safety Committee with an approved protocol (Chen-rDNA 15–45; 18–45; 21–45). All human sample work was performed under the guidelines of the Yale University Institutional Review Board with an approved protocol (HIC#2000020784). All animal work was performed under the guidelines of the Yale University Institutional Animal Care and Use Committee (IACUC) with approved protocols (Chen 2018-20068; 2021-20068).

Mouse models

Before all cancer-related experiments, each mouse was determined to be in good general health (bright, alert and responsive). Female and male mice, aged 8–12 weeks, were used for all experiments. The specific mouse strains used for this study included constitutive Cas9-expressing mice (also known as Rsky/Cas9β; Rosa26-Cas9-2A-EGFP in C57BL/6, B6), C57BL/6, B6 CD45.1 and NOD-*scid Il2rg*^{null} (NSG) mice. Each mouse strain was purchased from JAX and bred in house for in vivo tumor model experiments. All mice were housed with a controlled 12-h dark–light cycle at 22–24 °C and 40–60% humidity.

Cell lines and culture conditions

Cell lines were cultured in standard tissue culture conditions with commercially available cell lines and their engineered derivatives (see Supplementary Methods and Nature Portfolio Reporting Summary for details).

Mouse NK cell isolation and culture

Spleens were dissected from Rsky/Cas9β mice or C57BL/6J mice and placed into ice-cold PBS supplemented with 2% FBS. Lymphocytes were released by grinding organs through a 100-mm filter, washed with 2% FBS, treated with 1 ml of ACK lysis buffer (Lonza) per two spleens for 1–2 min at room temperature, neutralized with 2% FBS and filtered through 40-mm filters. Then, NK cells were purified using an EasySep Mouse NK Cell Isolation Kit (Stem Cell) according to the manufacturer's protocol. NK cells were cultured at a density of 5×10^6 cells per ml in plates or dishes with RPMI 1640 medium (Gibco) with 10% FBS, 2 mM L-glutamine, 200 U per ml penicillin–streptomycin (Gibco), 49 mM 2-mercaptoethanol (Sigma), 50 ng ml^{-1} IL-2 (Biolegend) and 50 ng ml^{-1} IL-15 (Biolegend).

Design, synthesis and cloning of AAV–SB-Surf-v2 CRISPR library

A list of proteins in the human surface proteome was obtained from Bausch-Fluck et al.[39]. The corresponding human genes were mapped to their mouse orthologous counterparts for a total of 2,867 genes. Exon sequences for these mouse genes were obtained through Ensembl Biomart, based on the mm10 genome assembly. Candidate Cas9 sgRNAs were then identified using FlashFry[40], following default settings and using the scoring metrics 'deonch2014ontarget', 'rank', 'minot', 'doench2016cfd' and 'dangerous'. With the resultant scoring matrix, sgRNAs were first filtered for those without high G+C content or poly(T) tracts and with exactly one match in the mm10 genome. The sgRNAs targeting a given gene were then ranked using the 'doench2014ontarget' and 'doench2016cfd' scores by first converting each score to nonparametric ranks, where high 'doench2014ontarget' scores correspond to high ranks and low 'doench2016cfd' scores correspond to high ranks. The two nonparametric ranks were then added together, weighing the 'doench2014ontarget' rank twice as heavily as the 'doench2016cfd' rank. For the final library design, all sgRNAs of the Brie library[41] were first selected and then the composite ranks described above were used to choose the top-scoring sgRNAs, up to a total of 20 sgRNAs per gene. The final set of on-target sgRNAs was composed of 56,911 sgRNAs targeting 2,863 mouse genes. A set of NTC sgRNAs was designed by generating 500,000 random 20-nucleotide sequences, followed by sgRNA scoring in FlashFry. The top 5,000 NTC sgRNAs were selected by choosing sgRNAs with a 'doench2016cfd' score < 0.2 and <100 total potential off-target sgRNAs (maximum of four mismatches). These 5,000 control sgRNAs were added to the library for a total of 61,911 sgRNAs. The oligo spacers for the surface-targeting gRNA library (Surf-v2) were generated by oligo array synthesis (CustomArray) and PCR-amplified and then oligos were cloned into double BbsI restriction digest sites of a custom sgRNA vector by Gibson Assembly (New England Biolabs (NEB)), after which assembly products were transformed into high-efficiency competent cells (Endura) by electroporation (estimated library coverage = 233.6-fold). The custom sgRNA vector used in this study was a hybrid AAV–SB-CRISPR plasmid for targeting primary mouse NK cells (AAV–SB100X) that was constructed by gBlock fragments (Integrated DNA Technologies (IDT)) followed by Gibson Assembly (NEB). The Surf-v2 library was cloned into the AAV–SB-CRISPR vector by pooled cloning to generate the AAV–SB-Surf-v2 plasmid library.

AAV production

The AAV–SB-Surf-v2 library was packaged similarly to our previously described approach[42] (see Supplementary Methods for details).

AAV–SB-Surf-v2 NK cell in vivo screens in syngeneic tumor models

The AAV–CRISPR screens were performed with >400× coverage, in which $>5 \times 10^7$ Cas9$^+$ NK cells were transduced with approximately 50% infectivity rate using the AAV–Surf-v2 viral library (0.5 infectivity × 5×10^7 cells/61,911 sgRNAs > 400-fold coverage). Naive NK cells were isolated from the spleens of Rsky/Cas9β mice. Syngeneic mouse models of melanoma, glioblastoma (GBM) and pancreatic cancer were set up with subcutaneous injections of 2×10^6 B16F10, 5×10^6 GL261 or 4×10^6 Pan02 cells, respectively. A syngeneic mouse model of breast cancer was established by fat-pad injections of 2×10^6 E0771 cells into C57BL/6J mice. AAV–Surf-v2-infected NK cells were adoptively transferred into tumor-burden mice by intravenous tail-vein injections. Four screen models were used with different endpoints: B16F10 melanoma and E0771 breast cancer models were killed at 20 dpi, while GL261 GBM and Pan02 pancreatic cancer models were killed at 27 dpi and 24 dpi, respectively. For B16F10 melanoma and E0771 breast cancer models, 4×10^6 AAV–Surf-v2-infected NK cells were injected into nine and ten tumor-burden mice, respectively; 2×10^6 AAV–Surf-v2-infected NK cells were injected into seven Pan02 pancreatic cancer and 11 GL261 GBM mouse models.

Tissue processing and gDNA extraction

gDNA was extracted from spleens, dissected tumors and preinjected cell pellets using the methods from a previous study[22] (see Supplementary Methods for details).

AAV–SB-CRISPR screen readout and sequencing

Library readout was performed by nested PCR reactions to decrease the effect of PCR amplification bias on the screen, following previous work[22] (see Supplementary Methods for details).

CRISPR KO screen data analyses

Raw sequencing data were demultiplexed and trimmed to the spacer sequences using Cutadapt (version 3.2)[43]. The spacers were then aligned to the reference sgRNA library using Bowtie (version 1.3.0)[44] and aligned reads were compiled into a count matrix that was further analyzed using MaGeCK-RRA[23] with the following parameters: norm-method = total and gene-lfc-method = alphamean. The native expression of genes in primary mouse NK cells was analyzed using the 18 NK samples from the ImmGen project (Gene Expression Omnibus (GEO) GSE122597)[24,45–48]. ImmGen NK count data were processed by

calculating the $\log_2$-transformed (pseudocount = 1) gene-averaged counts per million (cpm) and log expression > 0 was considered detectable expression. Screen data were used to intersect with ImmGen NK data using custom R scripts.

scRNA-seq of TINK cells

NK cells were isolated from the spleens of C57BL/6J mice and expanded through in vitro culture. Syngeneic mouse models of melanoma and breast cancer models were established with subcutaneous injections of native B16F10 or fat-pad injections of E0771 cells into C57BL/6J mice. NK cells were adoptively transferred into tumor-burden mice by intravenous tail-vein injections. At 7 and 15 days after NK cell transfer, one mouse was killed from each tumor model. Cells from spleens and tumors were collected from mice. For spleens, they were placed in ice-cold 2% FBS and mashed through a 100-µm filter. Splenocytes were washed once with 2% FBS. Tumors were minced into 1–3-mm^2 pieces using a scalpel and then digested using collagenase IV for 30–60 min at 37 °C. Tumor suspensions were filtered through a 100-µm cell strainer to remove large bulk masses. Red blood cells were lysed with 1 ml of ACK lysis buffer (Lonza) per spleen or 2 ml of ACK lysis buffer (Lonza) per tumor sample for 2–5 min at room temperature, which was followed by dilution with 10 ml of 2% FBS and passing the suspension through a 40-µm filter. Cells were resuspended in 2% FBS buffer, stained with anti-NK1.1–FITC (1:200) or anti-NKp46–PE (1:200) for 30 min on ice. $NKp46^+NK1.1^+$ double-positive NK cells were isolated by FACS using an FACSAria (BD). NK cells were then normalized to 1,000 cells per µl. Standard volumes of cell suspension were loaded to achieve a targeted cell recovery of 10,000 cells. The samples were subjected to 14 cycles of complementary DNA amplification. Following this, gene expression libraries were prepared according to the manufacturer's protocol (10x Genomics). All libraries were sequenced using a Novaseq 4000 (Illumina).

Single-cell transcriptomics data processing

scRNA-seq data were preprocessed with the Cell Ranger version 6.0.1 (10x Genomics) pipeline, using a standard pipeline that aligned reads to the mm10 mouse reference transcriptome and aggregated multiple datasets with the 'agg' function. The aggregated datasets were subsequently processed using the Seurat version 4.0.5 package for the R statistical programming language[49]. More specifically, each dataset was filtered to include cells with 200–2,500 RNA features, <5% mitochondrial RNA, 0.1% expression of *Kcnq1ot1* (representing low-quality cells)[50] and <5% combined expression of *Gm26917* and *Gm42418* (representing ribosomal RNA contamination)[51]. Each dataset was then log-normalized, scaled and integrated using Stuart et al.'s method using reciprocal principal component analysis (PCA) dimensional reduction, 2,000 anchors and $k = 20$ (ref. 25).

Integrated data were rescaled and dimensional reduction was performed by UMAP[26] using the first 27 dimensions from PCA, which were chosen by the inflection point of an elbow plot. Cells were clustered in low-dimensional space by generating a shared nearest neighbor graph ($k = 20$, first 27 principal components (PCs)) with modularity optimization using the Louvain algorithm with a multilevel refinement algorithm (resolution = 0.4) based on the best spatial separation of major immune cell populations according to *Cd3e*, *Cd14*, *Cd19*, *Sdc1*, *Adgre1*, *Ncr1*, *Hbb-bs*, *Gypa*, *Pmel*, *H2-Aa*, *Ly6g* and *Ptprc* expression (>10% of cell population with >1 log-scale expression). NK cells were subset, rescaled, visualized by UMAP (first 20 PCs used) and clustered with an optimal resolution of 0.4 on the basis of maximal average silhouette width and minimal within-cluster sum-of-squares values when comparing resolutions from 0.2 to 1.0 at 0.1 increments. These same markers were also used to label the cell clusters as specific NK populations using the same method as above. The labeled NK cell populations were assessed for within-cluster homogeneity by performing Wilcoxon rank-sum analyses of scaled expression data in each cluster compared to all other cells, selecting the top 100 DE genes for each cluster (FDR-adjusted P value < 0.01, absolute $\log_2$(FC) > 1 and cluster detection rate > 20%) and determining the presence of discreet cluster-specific transcriptional patterns by hierarchical clustering and heat-map visualization.

Single-cell DE analyses

DE analyses of single-cell transcriptomics data were performed using a custom R pipeline, as previously described[52]. Briefly, raw single-cell data were filtered to include genes with detectable expression in ≥5% of cells and cells that expressed ≥10% of the filtered genes; then, filtered data were fit to gamma–Poisson generalized log-linear models (GLMs) using the deconvolution method for the calculation of size factors[53,54]. DE analyses of fitted data were then assessed by empirical Bayes quasi-likelihood F tests. GLM fitting and DE were performed using the glmGamPoi package for R[53], assessing tumor infiltration as the coefficient. For subsequent analyses, DE genes were those with an FDR-adjusted P value < 0.01 and an absolute $\log_2$(FC) > 1.

Lentivirus production

Lentivirus was produced using low-passage HEK239FT or HEK293T cells (see Supplementary Methods for details).

Lentiviral transduction of NK92 cells

Lentiviral transduction of NK92 cells was performed using spin infection at 32 °C at 900*g* for 90 min (see Supplementary Methods for details).

CRISPR gene editing in NK92 cells and human primary NK cells

The CRISPR-mediated gene editing of *CALHM2* and *AAVS1* (control) was performed by electroporation. Briefly, crRNA and *trans*-activating crRNA (tracrRNA) were mixed in a 1:1 ratio (final concentration 50 µM), heated at 95 °C for 5 min in a thermal cycler and then cooled to room temperature. Next, 3 µl of HiFi Cas9 protein (62 µM; IDT) was mixed with 2 µl of buffer R for each reaction (Neon Transfection System Kit, Invitrogen) and then mixed with 5 µl of the annealed crRNA–tracrRNA duplex, which was then incubated at room temperature for 15 min. For each reaction, 3×10^6 NK92 cells or human primary NK cells were resuspended in 90 µl of buffer R and 10 µl of RNP complex. A 100-µl cell–RNP mixture was loaded into the Neon Pipette without bubbles and electroporation was performed at 1,600 V for 10 ms with three pulses. Cells were immediately transferred to a 24-well plate with prewarmed medium after electroporation. The KO or protein knockdown efficiency for each target was examined after 5 days by T7E1 assays and western blots.

Parental NK92 and CAR-NK92 cytotoxicity assay

To detect the cytotoxic capabilities of *CALHM2*-KO parental NK92 and CAR-NK92 cells, cancer cell lines (K562-GL, MDA-MB-231-PL, HT29-GL, MM.1R-PL, MM.1R-PL-BCMA-OE, MCF-7-PL and MCF-7-PL-HER2-OE) were seeded in a 96-well plate. Subsequently, cocultures with different ratios of effector (NK92 cell or CAR-NK92 cell) to target (cancer cells) were set up. Cytolysis was then measured by adding 150 µg ml^{-1} D-luciferin (PerkinElmer) using a multichannel pipette. Luciferase bioluminescence was measured with a luminometer (PerkinElmer).

CD107a degranulation assay

CAR-NK92 cells and NK92 cells were pelleted and resuspended with fresh culture medium, supplemented with 2 nM monensin and anti-CD107a-PE antibody (BioLegend) (1:1,000 dilution), and then stimulated with MCF-7-PL, MCF-7-PL-HER2-OE or HT29 cells at an E:T ratio of 1:1 or 1:2 for 2, 4 and 6 h. At the end of each coculture, CAR-NK92 and NK92 cells were washed with PBS and stained with anti-CD56–FITC (1:200) or anti-CD56–APC (1:200) for 30 min on ice. Cells were analyzed using a BD FACSAria or Cytek Aurora.

Western blots
Western blots were performed using standard molecular biology protocols (see Supplementary Methods for details) with commercially available antibodies (see Nature Portfolio Reporting Summary and Supplementary Information).

In vivo antitumor efficacy testing
NSG mice were purchased from JAX and bred in house. First, 8–12-week-old male mice were inoculated with 2×10^6 HT29-GL cells through subcutaneous injection. After 12 days, 5×10^6 *AAVS1*-KO or *CALHM2*-KO anti-HER2-CAR-hIL-2-NK92 cells were injected intravenously into tumor-burden mice. Female mice were used in an independent cohort leading to similar observations. In the following days, CAR-NK92 cells were injected once a week for three sequential weeks. Treatment doses and time points were labeled in the appropriate figures. Tumor volumes were measured by caliper and calculated with the following formula: volume = $\pi/6 \times$ length $\times$ width $\times$ height. All mice were killed once they reached humane endpoints according to IACUC-approved protocols.

In vivo tumor infiltration assay of *Calhm2*-KO mouse NK cells
Syngeneic mouse models of breast cancer were established by injecting 1×10^6 E0771 cells into the fat pads of CD45.1 mice. Tumor-bearing mice were randomly assembled into different treatment groups. At the same time, naive NK cells were isolated from the spleens of Cas9-expressing mice. Then, 6 days later, NK cells were transduced separately with AAV-*Calhm2* and AAV-pLY017b vectors. The NK cells were cultured for an additional 4 days in vitro before being adoptively transferred into tumor-burden mice by tail-vein injection (7×10^6 NK cells per mouse). All mice were killed 2 days later. Spleens and tumors were dissected and used for analysis.

In vivo tumor infiltration assay of *CALHM2*-KO CAR-NK92 cells
NSG mice were purchased from JAX and bred in house. First, 8–12-week-old female mice were inoculated with 4×10^6 HT29-GL cells through subcutaneous injection. After 19 days, tumor-bearing mice were randomized into two groups that were treated with 1×10^7 *AAVS1*-KO or *CALHM2*-KO anti-HER2-CAR-hIL-2-NK92 cells intravenously. Mice were killed at 21 and 28 dpi and the tumors and spleens were collected for flow cytometry analyses.

Isolation of splenocytes and tumor-infiltrating lymphocytes
Mice were killed at the indicated time points. Tumors and spleens were collected and kept in ice-cold 2% FBS. Spleens were mashed through a 100-µm filter and then washed once with 2% FBS. Tumors were minced into 1–3-mm^2 pieces using a scalpel, digested using collagenase IV for 30–60 min at 37 °C and then filtered through a 100-µm cell strainer to remove large masses. Red blood cells were lysed with ACK lysis buffer (Lonza) (1 ml per spleen or 2 ml per tumor) for 2–5 min at room temperature, diluted with 10 ml of 2% FBS and then passed through a 40-µm filter. Single-cell suspensions were resuspended in 2% FBS buffer and counted for flow cytometry staining.

FACS analysis of TINK cells
FACS analyses were performed using standard immunology protocols (see Supplementary Methods for details) with commercially available antibodies (see Nature Portfolio Reporting Summary and Supplementary Information).

Cell proliferation assay
Cells were collected, counted, adjusted to 1×10^7 cells per ml with CellTrace Far Red staining (1:1,000 dilution) staining solution and incubated at 37 °C for 20 min. Complete cell culture medium was then added before mixing and incubating at 37 °C for 5 min. Cells were pelleted and resuspended in fresh, prewarmed complete culture medium.

Human primary NK cell in vitro expansion and purification
Primary NK cells were expanded and purified from peripheral blood mononuclear cells (PBMCs) collected from healthy individuals through bead selection. Initially, feeder cells were prepared from K562 cells, transduced with 4-1BBL, membrane-bound IL-15 and membrane-bound IL-21 and treated with 20 µg ml^{-1} mitomycin C at 37 °C for 30 min. After treatment, the mitomycin C-treated feeder cells were washed twice with PBS and once with complete RPMI medium. PBMCs were then cocultured with feeder cells at a 1:1 ratio of feeder cells to PBMCs. After 7 days of culture, cells were harvested, stained with APC–anti-CD3 antibody for 20 min (5 µl per 1×10^6 cells) at 4 °C, stained with anti-APC MicroBeads for another 20 min at 4 °C, washed, positively selected with an MACS LS column (Miltenyi Biotech) and then cultured in Iscove's modified Dulbecco's medium, supplemented with 10% FBS, 1% penicillin–streptomycin, 5 ng ml^{-1} IL-15 and 400 U of IL-2.

Human primary NK cell cytotoxicity assay
To assess the cytotoxic capabilities of *CALHM2*-KO human primary NK cells, cancer cell lines (K562-GL, MCF-7-PL and HT29-GL) were seeded in a 96-well plate and cocultured with the NK cells at different E:T ratios. Cytolysis was evaluated by adding 150 µg ml^{-1} D-luciferin (PerkinElmer) before measuring luciferase bioluminescence with a luminometer (PerkinElmer).

Human primary NK cell CD107a degranulation assay
Human primary NK cells were resuspended in fresh culture medium supplemented with 2 nM monensin and anti-CD107a–PE antibody (BioLegend) at a 1:1,000 dilution. The cells were then cocultured with K562 and HT29 cells at an E:T ratio of 1:2 (NK cells to cancer cells) for 2, 4 and 6 h. After each coculture period, primary NK cells were washed with MACS buffer and stained with anti-CD56–FITC (1:200) or anti-CD56–APC (1:200) for 30 min on ice. Subsequently, the cells were analyzed using a Cytek Aurora flow cytometer.

Human primary NK cell cytokine secretion assay
CALHM2-KO and *AAVS1*-KO primary NK cells were stimulated with cancer cell lines (K562-GL, MCF-7-PL or HT29-GL) at an E:T ratio of 1:5. Following a 12-h incubation period, the supernatants were harvested and quantified using human IFNγ and TNFα ELISA assays, following the manufacturer's instructions.

CALHM2 rescue experiments
CALHM2 mRNA synthesis was performed using the HiScribe T7 ARCA mRNA Kit (with tailing) from NEB, followed by purification with the Monarch RNA Cleanup Kit (50 µg), according to the manufacturer's instructions. The *CALHM2* mRNA was then introduced to the cells by electroporation. Specifically, *CALHM2*-KO anti-HER2-CAR-hIL-2-NK92 cells (3×10^6 cells per reaction) were suspended in 90 µl of buffer R, to which 10 µl of *CALHM2* mRNA (1 µg μl^{-1}) was added. The cell–mRNA mixture (100 µl) was carefully loaded into the Neon Pipette without introducing bubbles and electroporation was performed at 1,600 V for 10 ms with three pulses. After electroporation, cells were immediately transferred to prewarmed medium in a six-well plate. Overexpression of CALHM2 was assessed by western blot at 18 h after electroporation. Subsequently, the cells were used for cytotoxicity assays and degranulation assays at 24–48 h after electroporation.

Human primary NK mRNA-seq
CALHM2 and *AAVS1* were knocked out in primary human NK cells (from donor 1) using the Cas9 RNP complex system. The resulting KO and control cells at 4 days after electroporation were either collected (unstimulated condition) or cocultured with HT29-GL cells and then collected using the beads method for mRNA-seq library prep. The mRNA samples were extracted with RNeasy plus kit (Qiagen). The mRNA-seq library preparations were performed using the NEBNext Ultra RNA Library

Prep Kit and multiplexed using barcoded primers provided by NEBNext Multiplex Oligos for Illumina (index primer set 2). The libraries were then sequenced using a Novaseq 4000 (Illumina).

Bulk mRNA-seq data analysis

Bulk mRNA-seq was performed in *AAVS1*-KO and *CALHM2*-KO human primary NK cells with or without cancer stimulation. Raw sequencing data were filtered and adaptors were removed by Cutadapt (version 3.2)[43] in paired-end mode, clipping Illumina TruSeq adaptors with the following settings: -m36 -e0.2. Trimmed, filtered reads were then aligned to the human transcriptome (GRCh38 Gencode version 96) using Kallisto version 0.45.0 with default settings[55]. Aligned reads were imported in R using the EdgeR package[35] and the data were processed by removing low-expression transcripts with the filterByExpr command (default settings), normalized by the trimmed mean of *M* values method[56]. Next, DE analyses were performed using likelihood ratio tests[35]. For subsequent analyses, DE genes were those with an FDR-adjusted *P* value < 0.05 and an absolute $\log_2$(FC) > 1.0. For pathway analyses, DE genes from unstimulated and stimulated analysis were clustered (Ward D2 algorithm with Euclidean distances) across all samples using the transcript $\log_2$(cpm). Clustered genes were analyzed by the g:Profiler2 R package with Gene Ontology (GO) terms for biological processes and Reactome pathways with known genes as the analysis domain[57,58]. Enrichment analysis results were filtered to keep significant GO terms (adjusted *P* value (g:Profiler gSCS method) < 0.01) while excluding vague and poorly matched GO terms (<750 term genes; term overlaps ≥ 2 DE genes).

Meta-pathway analyses

Meta-pathway analyses were performed using a modified pipeline of a previously described strategy[52]. First, upregulated or downregulated DE genes were sorted by *P* value and used as input for gene set enrichment analyses by the g:Profiler2 R package with GO terms for biological processes and known genes as the analysis domain[57,58]. Enrichment analysis results were filtered to keep significant GO terms (adjusted *P* value (g:Profiler gSCS method) < 0.01) while excluding vague and poorly matched GO terms (<750 term genes; term overlaps ≥ 2 DE genes). If there were more than two filtered terms, analysis results were clustered into meta-pathways by generating an undirected network with a Fruchterman–Reingold layout, with edges weighted by similarity coefficients between genes of each term (coefficient = Jaccard + overlap of genes between GO terms; coefficient threshold = 0.375). The terms were grouped by Leiden clustering (modularity optimization method, 500 iterations) using the iGraph, network and sna R packages. A representative meta-pathway was chosen from the terms of each cluster as the term with the highest precision value that was well represented by the input gene list (term size > 50 total genes; overlapping number of DE genes and terms > 10th percentile of filtered terms). The resolution for Leiden clustering was empirically optimized by the dataset type to limit the occurrence of redundant meta-pathways (resolution of 1.4 for bulk RNA-seq analyses and 1.2 for the screen and scRNA-seq analyses). For visualization, the five most significant meta-pathways were displayed as network plots with all clustered terms shown.

Sample size determination

Sample size was determined according to the lab's prior work or from published studies of similar scope within the appropriate fields.

Replication

The number of biological replicates (typically n ≥ 3) is indicated in the figure legends. Key findings (not related to next-generation sequencing (NGS)) were replicated in at least two independent experiments. NGS experiments were performed with biological replications as indicated in the manuscript.

Randomization and blinding statements

Regular in vitro experiments were not randomized or blinded. Mouse experiments were randomized by using littermates and blinded using generic cage barcodes and ear tags, where applicable. High-throughput experiments and analyses were blinded by barcoded metadata.

Standard statistical analysis

Standard statistical analyses were performed using common statistical methods with GraphPad Prism, Excel and R. Different levels of statistical significance were assessed on the basis of specific *P* values and type I error cutoffs (0.05, 0.01, 0.001 and 0.0001). Further details of statistical tests were provided in the figure legends and/or Supplementary Information.

Data collection summary

Flow cytometry data were collected using a BD FACSAria and a Cytek Aurora.

All deep sequencing data were collected using Illumina Sequencers at the Yale Center for Genome Analysis (YCGA). Coculture killing assay data were collected using a PE Envision Plate Reader.

Data analysis summary

Flow cytometry data were analyzed using FlowJo version 10.7.
All basic statistical analyses were conducted with Prism 9.
NGS analyses were performed using custom codes.

Reporting summary

Further information on research design is available in the Nature Portfolio Reporting Summary linked to this article.

Data availability

All generated data and analysis results for this study are included in this article and its supplementary information files. Specifically, source data and statistics for non-high-throughput experiments are provided in Supplementary Datasets and Source Data. Processed data and raw sequencing data are available from the GEO under accession numbers GSE262707, GSE262708 and GSE262760, all under the GSE262709 super-series (https://www.ncbi.nlm.nih.gov/geo/query/acc.cgi?acc=GSE262709). Original cell lines are available from the commercial sources listed in the Supplementary Information. Source data are provided with this paper. Other relevant information or data are available from the corresponding authors upon reasonable request.

Code availability

The code used for data analysis and the generation of figures related to this study is available from the Supplementary Dataset 6 and GitHub (https://github.com/Prenauer/TumorInfiltrating_CAR-NK)[59].

References

39. Bausch-Fluck, D. et al. The in silico human surfaceome. *Proc. Natl Acad. Sci. USA* **115**, E10988–E10997 (2018).
40. McKenna, A. & Shendure, J. FlashFry: a fast and flexible tool for large-scale CRISPR target design. *BMC Biol.* **16**, 74 (2018).
41. Doench, J. G. et al. Optimized sgRNA design to maximize activity and minimize off-target effects of CRISPR–Cas9. *Nat. Biotechnol.* **34**, 184–191 (2016).
42. Ye, L. et al. A genome-scale gain-of-function CRISPR screen in CD8 T cells identifies proline metabolism as a means to enhance CAR-T therapy. *Cell Metab.* **34**, 595–614 (2022).
43. Martin, M. Cutadapt removes adapter sequences from high-throughput sequencing reads. *EMBnet J.* **17**, 10–12 (2011).
44. Langmead, B., Trapnell, C., Pop, M. & Salzberg, S. L. Ultrafast and memory-efficient alignment of short DNA sequences to the human genome. *Genome Biol.* **10**, R25 (2009).

45. Aguilar, S. V. et al. ImmGen at 15. *Nat. Immunol.* **21**, 700–703 (2020).
46. Gal-Oz, S. T. et al. ImmGen report: sexual dimorphism in the immune system transcriptome. *Nat. Commun.* **10**, 4295 (2019).
47. Zemmour, D., Goldrath, A., Kronenberg, M., Kang, J. S. & Benoist, C. The ImmGen consortium OpenSource T cell project. *Nat. Immunol.* **23**, 643–644 (2022).
48. Bezman, N. A. et al. Molecular definition of the identity and activation of natural killer cells. *Nat. Immunol.* **13**, 1000–1009 (2012).
49. Satija, R., Farrell, J. A., Gennert, D., Schier, A. F. & Regev, A. Spatial reconstruction of single-cell gene expression data. *Nat. Biotechnol.* **33**, 495–502 (2015).
50. Jordão, M. J. C. et al. Single-cell profiling identifies myeloid cell subsets with distinct fates during neuroinflammation. *Science* **363**, eaat7554 (2019).
51. Liu, Y. et al. Single-cell profiling reveals divergent, globally patterned immune responses in murine skin inflammation. *iScience* **23**, 101582 (2020).
52. Peng, L. et al. Variant-specific vaccination induces systems immune responses and potent in vivo protection against SARS-CoV-2. *Cell Rep. Med.* **3**, 100634 (2022).
53. Ahlmann-Eltze, C. & Huber, W. glmGamPoi: fitting gamma–Poisson generalized linear models on single cell count data. *Bioinformatics* **36**, 5701–5702 (2020).
54. Soneson, C. & Robinson, M. D. Bias, robustness and scalability in single-cell differential expression analysis. *Nat. Methods* **15**, 255–261 (2018).
55. Bray, N. L., Pimentel, H., Melsted, P. & Pachter, L. Near-optimal probabilistic RNA-seq quantification. *Nat. Biotechnol.* **34**, 525–527 (2016).
56. Robinson, M. D. & Oshlack, A. A scaling normalization method for differential expression analysis of RNA-seq data. *Genome Biol.* **11**, R25 (2010).
57. Kolberg, L., Kerimov, N., Peterson, H. & Alasoo, K. Co-expression analysis reveals interpretable gene modules controlled by trans-acting genetic variants. *eLife* **9**, e58705 (2020).
58. Raudvere, U. et al. g:Profiler: a web server for functional enrichment analysis and conversions of gene lists (2019 update). *Nucleic Acids Res.* **47**, W191–W198 (2019).
59. Peng, L. et al. In vivo AAV–SB-CRISPR screens of tumor-infiltrating primary NK cells identify genetic checkpoints of CAR-NK therapy. *GitHub* https://github.com/Prenauer/TumorInfiltrating_CAR-NK (2024).

Acknowledgements

We thank all members of the Chen laboratory, as well as our colleagues in the Department of Genetics, Systems Biology Institute, Cancer Systems Biology Center, MCGD Program, Immunobiology Program, BBS Program, Yale Cancer Center (YCC), Yale Stem Cell Center, RNA Center and Center for Biomedical Data Sciences at Yale for assistance and/or discussion. We thank the YCGA, Yale Center for Molecular Discovery, High-Performance Computing Center, West Campus Analytical Chemistry Core, West Campus Mass Spec Core and Keck Biotechnology Resource Laboratory at Yale for technical support. S.C. is supported by a Yale SBI/Genetics Startup Fund, a Cancer Research Institute Lloyd J. Old STAR Award (CRI4964), the National Institutes of Health (NIH) National Cancer Institute (NCI) (DP2CA238295, R01CA231112 and 1R33CA281702), the Department of Defense (W81XWH-20-1-0072, W81XWH-21-1-0514, HT9425-23-1-0472 and HT9425-23-1-0860), the Alliance for Cancer Gene Therapy (ACGT), the Pershing Square Sohn Cancer Research Alliance, the Sontag Foundation, Dexter Lu, the Ludwig Family Foundation, the Blavatnik Family Foundation and the Chenevert Family Foundation. P.A.R. is supported by a Yale PhD training grant from NIH (T32GM007499), the Lo Fellowship of Excellence of Stem Cell Research, the NCI diversity supplement and the YCC T32 fellowship program. G.S. is supported by a Vita-Salute San Raffaele University fellowship. J.J.P. is supported by an NIH Medical Scientist Training Program (MSTP) training grant (T32GM007205). R.D.C. is supported by an NIH MSTP training grant (T32GM007205) and National Research Service Award fellowship (F30CA250249).

Author contributions

S.C. conceptualized the study and designed it with L.P., P.A.R. and L. Ye. L.P. performed most experiments. P.A.R. performed most NGS analyses. L. Ye coperformed the screen and single-cell experiments and supported or supervised certain validation experiments. G.S., L. Yang, Y. Zou, Z.F., Q.L., M.B., A.S., Yueqi Zhang and S.Z.L. assisted with experiments. J.J.P. and Yongzhan Zhang performed certain NGS analyses. R.D.C. designed the Surf-v2 library. L.P., P.A.R. and S.C. prepared the manuscript with input from all authors. S.C. secured funding and supervised the work.

Competing interests

A patent was filed by Yale University regarding the data in this study, which was licensed to Cellinfinity Bio, a Yale biotech startup founded by S.C. S.C. is also a founder or cofounder of EvolveImmune, NumericGlobal, MagicTime Med and Chen Consulting, all unrelated to this study. The other authors declare no competing interests.

Additional information

Supplementary information The online version contains supplementary material available at https://doi.org/10.1038/s41587-024-02282-4.

Correspondence and requests for materials should be addressed to Lupeng Ye or Sidi Chen.

Peer review information *Nature Biotechnology* thanks the anonymous reviewer(s) for their contribution to the peer review of this work.

nature portfolio

Corresponding author(s): Sidi Chen

Last updated by author(s): May 5, 2024

Reporting Summary

Nature Portfolio wishes to improve the reproducibility of the work that we publish. This form provides structure for consistency and transparency in reporting. For further information on Nature Portfolio policies, see our Editorial Policies and the Editorial Policy Checklist.

Statistics

For all statistical analyses, confirm that the following items are present in the figure legend, table legend, main text, or Methods section.

n/a	Confirmed	
☐	☒	The exact sample size (*n*) for each experimental group/condition, given as a discrete number and unit of measurement
☐	☒	A statement on whether measurements were taken from distinct samples or whether the same sample was measured repeatedly
☐	☒	The statistical test(s) used AND whether they are one- or two-sided *Only common tests should be described solely by name; describe more complex techniques in the Methods section.*
☐	☒	A description of all covariates tested
☐	☒	A description of any assumptions or corrections, such as tests of normality and adjustment for multiple comparisons
☐	☒	A full description of the statistical parameters including central tendency (e.g. means) or other basic estimates (e.g. regression coefficient) AND variation (e.g. standard deviation) or associated estimates of uncertainty (e.g. confidence intervals)
☐	☒	For null hypothesis testing, the test statistic (e.g. *F*, *t*, *r*) with confidence intervals, effect sizes, degrees of freedom and *P* value noted *Give P values as exact values whenever suitable.*
☒	☐	For Bayesian analysis, information on the choice of priors and Markov chain Monte Carlo settings
☐	☒	For hierarchical and complex designs, identification of the appropriate level for tests and full reporting of outcomes
☐	☒	Estimates of effect sizes (e.g. Cohen's *d*, Pearson's *r*), indicating how they were calculated

Our web collection on statistics for biologists contains articles on many of the points above.

Software and code

Policy information about availability of computer code

Data collection	Flow cytometry data was collected by BD FACSAria; All deep sequencing data were collected using Illumina Sequencers at Yale Center for Genome Analysis (YCGA). Co-culture killing assay data were collected with PE Envision Plate Reader. Western blot gel imaging were collected with Bio-Rad's New ChemiDoc Touch Imaging System.
Data analysis	Flow cytometry data were analyzed by FlowJo v.10.7. All simple statistical analyses were done with Prism 9. All NGS analyses were performed using custom codes. Quantification of Western blot gel imaging with Image J

For manuscripts utilizing custom algorithms or software that are central to the research but not yet described in published literature, software must be made available to editors and reviewers. We strongly encourage code deposition in a community repository (e.g. GitHub). See the Nature Portfolio guidelines for submitting code & software for further information.

Data

Policy information about availability of data

All manuscripts must include a data availability statement. This statement should provide the following information, where applicable:

- Accession codes, unique identifiers, or web links for publicly available datasets
- A description of any restrictions on data availability
- For clinical datasets or third party data, please ensure that the statement adheres to our policy

All generated data and analysis information/results for this study is included in this article and its supplementary information files. Specifically, source data and

statistics for non-high-throughput experiments are provided in Supplemental Tables. Processed data and raw sequencing data are available at the Gene Expression Omnibus (GEO) with following accession numbers: GSE262707, GSE262708, and GSE262760, all under the GSE262709 super-series (https://www.ncbi.nlm.nih.gov/geo/query/acc.cgi?acc=GSE262709) 60. Original cell lines are available at the commercial sources listed in supplementary information files. Other relevant information or data are available from the corresponding author upon reasonable request.

Field-specific reporting

Please select the one below that is the best fit for your research. If you are not sure, read the appropriate sections before making your selection.

☒ Life sciences ☐ Behavioural & social sciences ☐ Ecological, evolutionary & environmental sciences

For a reference copy of the document with all sections, see nature.com/documents/nr-reporting-summary-flat.pdf

Life sciences study design

All studies must disclose on these points even when the disclosure is negative.

Sample size	Sample size was determined according to the lab's prior work or similar approaches in the field.
Data exclusions	No data was excluded.
Replication	Number of biological replicates (usually n >= 3) are indicated in the figure legends. Key findings (non-NGS) were replicated in at least two independent experiments. NGS experiments were performed with biological replications as indicated in the manuscript.
Randomization	Regular in vitro experiments were not randomized or blinded. Mouse experiments were randomized by using littermates, and blinded using generic cage barcodes and eartags where applicable. High-throughput experiments and analyses were blinded by barcoded metadata.
Blinding	Regular in vitro experiments were not randomized or blinded. Mouse experiments were randomized by using littermates, and blinded using generic cage barcodes and eartags where applicable. High-throughput experiments and analyses were blinded by barcoded metadata.

Reporting for specific materials, systems and methods

We require information from authors about some types of materials, experimental systems and methods used in many studies. Here, indicate whether each material, system or method listed is relevant to your study. If you are not sure if a list item applies to your research, read the appropriate section before selecting a response.

Materials & experimental systems

n/a	Involved in the study	
☐	☒	Antibodies
☐	☒	Eukaryotic cell lines
☒	☐	Palaeontology and archaeology
☐	☒	Animals and other organisms
☒	☐	Human research participants
☒	☐	Clinical data
☒	☐	Dual use research of concern

Methods

n/a	Involved in the study	
☒	☐	ChIP-seq
☐	☒	Flow cytometry
☒	☐	MRI-based neuroimaging

Antibodies

Antibodies used	PE anti-DYKDDDDK Tag Antibody (L5), Biolegend,Cat#637310; FITC anti-mouse NK-1.1 Antibody (S17016D),Biolegend,Cat#156508;PE anti-mouse CD335 (NKp46) Antibody (29A1.4), Biolegend,Cat#137604; FITC anti-human CD56 (NCAM) Antibody (5.1H11), Biolegend, Cat#362546; PE anti-human CD107a (LAMP-1) Antibody (H4A3), Biolegend, Cat#328608;α-CALHM2 polyclonal antibody , Invitrogen, PA5-53219;goat anti-Rabbit IgG (H+L) secondary antibody with HRP,Invitrogen, 65-6120;α-Vinculin Recombinant Rabbit Monoclonal antibody (42H89L44),Invitrogen, 700062;FITC anti-mouse CD335 (NKp46) Antibody (29A1.4), Biolegend,Cat#137605;BV421 anti-mouse CD45.2 (104), Biolegend,Cat#109831;PE/Cyanine7 anti-mouse CD3 Antibody (17A2),Biolegend,Cat#100219;TruStain FcX™ PLUS (anti-mouse CD16/32) Antibody (S17011E) ,Biolegend,Cat#156603;APC anti-human CD56 (NCAM) Antibody (HCD56),Biolegend,Cat#318310;APC anti-human CD3 Antibody (OKT3),Biolegend,Cat#317318. The standard dilution for all flow cytometry antibodies used in surface staining is 1:200. Specifically, for the TruStain FcX™ PLUS (anti-mouse CD16/32) Antibody, the recommended concentration is 0.25 µg of antibody per 10^6 cells, with a staining volume of 100 µl.
Validation	Concentration of antibodies were validated based on manufacturing instructions. α-CALHM2 polyclonal antibody (Invitrogen, PA5-53219) can be used for mouse and human Calhm2/CALHM2 protein staining with a dilution ratio of 1 : 400. Vinculin Recombinant Rabbit Monoclonal antibody (42H89L44) (Invitrogen, 700062) can be used for mouse and human Vinculin/VINCULIN protein staining with a dilution ratio of 1 : 400.

Eukaryotic cell lines

Policy information about cell lines

Cell line source(s)	K562 ATCC Catalog Number: CCL-243 ™ HEK293FT ThermoFisher Catalog Number : R70007K562 HEK293T ATCC Catalog Number: CRL-3216™ YAC-1 ATCC Catalog Number:TIB-160 ™ MCF-7 ATCC Catalog Number: HTB-22 E0771 CH3 Catalog Number: 940001 MB-MDA-231 ATCC Catalog Number: HTB-26 NK92 ATCC Catalog Number: CRL-2407™ HT29 ATCC Catalog Number : HTB-38 MM.1R ATCC Catalog Number: CRL-2975 B16F10 ATCC Catalog Number: CRL-6475™ GL261 ATCC Catalog Number: HB-12317™ Pan02 ATCC Catalog Number: CRL-2553™
Authentication	Cell lines were authenticated by the commercial vendor through morphology.
Mycoplasma contamination	I confirm that all the cell lines have tested and showed no mycoplasma contamination.
Commonly misidentified lines (See ICLAC register)	No commonly misidentified lines were used in the study.

Animals and other organisms

Policy information about studies involving animals; ARRIVE guidelines recommended for reporting animal research

Laboratory animals	Rosa26-Cas9-2A-EGFP constitutive expressed mice (Cas9 mice, also noted as Rsky/Cas9 mice) were used in this study. C57BL/6 and NOD-scid IL2Rgammanull (NSG) mice were purchased from JAX and bred in-house for in vivo tumor model and NK92 cell based therapeutic efficacy testing experiments. Mice, both female and male, aged 8-12 weeks were used for experiments. CD45.1 mice were purchased from JAX
Wild animals	no wild animals were used in the study.
Field-collected samples	no field collected samples were used in the study
Ethics oversight	This study has received institutional regulatory approval. All recombinant DNA and biosafety work were performed under the guidelines of Yale Environment, Health and Safety (EHS) Committee with an approved protocol (Chen-rDNA 15-45; 18-45; 21-45). All human sample work was performed under the guidelines of Yale University Institutional Review Board (IRB) with an approved protocol (HIC#2000020784). All animal work was performed under the guidelines of Yale University Institutional Animal Care and Use Committee (IACUC) with approved protocols (Chen 2018-20068; 2021-20068).

Note that full information on the approval of the study protocol must also be provided in the manuscript.

Flow Cytometry

Plots

Confirm that:

☒ The axis labels state the marker and fluorochrome used (e.g. CD4-FITC).

☒ The axis scales are clearly visible. Include numbers along axes only for bottom left plot of group (a 'group' is an analysis of identical markers).

☒ All plots are contour plots with outliers or pseudocolor plots.

☒ A numerical value for number of cells or percentage (with statistics) is provided.

Methodology

Sample preparation	Surface staining for flow cytometry and cell sorting was performed by pelleting cells and resuspending in 100 µL of MACS Buffer (5% BSA in PBS, and 2mM EDTA) with antibodies (1:200 dilution) for 30 minutes at 4C in the dark. Cells were washed once in MACS buffer before resuspension. For intracellular staining, cells were fixed and permeabilized by fixation/permeabilization solution (BD) for 20 min. and resuspending in 100 µL of permeabilization/wash Bufferwith antibodies (1:1000 dilution) for 30 minutes at 4C in the dark. Cells were washed three times in MACS buffer before resuspension.
Instrument	Flow cytometric analysis was performed on an BD FACSAria II or thermo Attune™ NxT or Cytek Aurora Analyzer.
Software	FlowJo v.10.7.1 was used for flow ctyometry data analysis.

Cell population abundance	CAR-NK92 cells were selected with puromycin. The survived cells were re-measured by FACS to confirm the purity (>90%).
Gating strategy	A lymphocyte gate was defined first from FSC-A v SSC-A. Singlet gates were then defined on FSC-H v FSC-W. Additional gating was performed as described in figure and extended data legends for individual experiments.

☒ Tick this box to confirm that a figure exemplifying the gating strategy is provided in the Supplementary Information.